REPORT

OPEN ACCESS

Self-calibrating multiplexed microneedle electrode array for continuous mapping of subcutaneous multi-analytes in diabetes

Xiangling Li,[1,2,*] Shantao Zheng,[1] Mengyi He,[1] Xinshuo Huang,[1] Cheng Yang,[1] Jingshan Mo,[1] Jingbo Yang,[2] Chengduan Yang,[1] Huijiuan Chen,[1] and Xi Xie[1,2,*]

*Correspondence: lixiangling05@outlook.com (X.L.); xiexi27@mail.sysu.edu.cn (X.X.)

Received: May 3, 2024; Accepted: December 26, 2024; Published Online: January 25, 2025; https://doi.org/10.1016/j.xinn.2024.100781

GRAPHICAL ABSTRACT

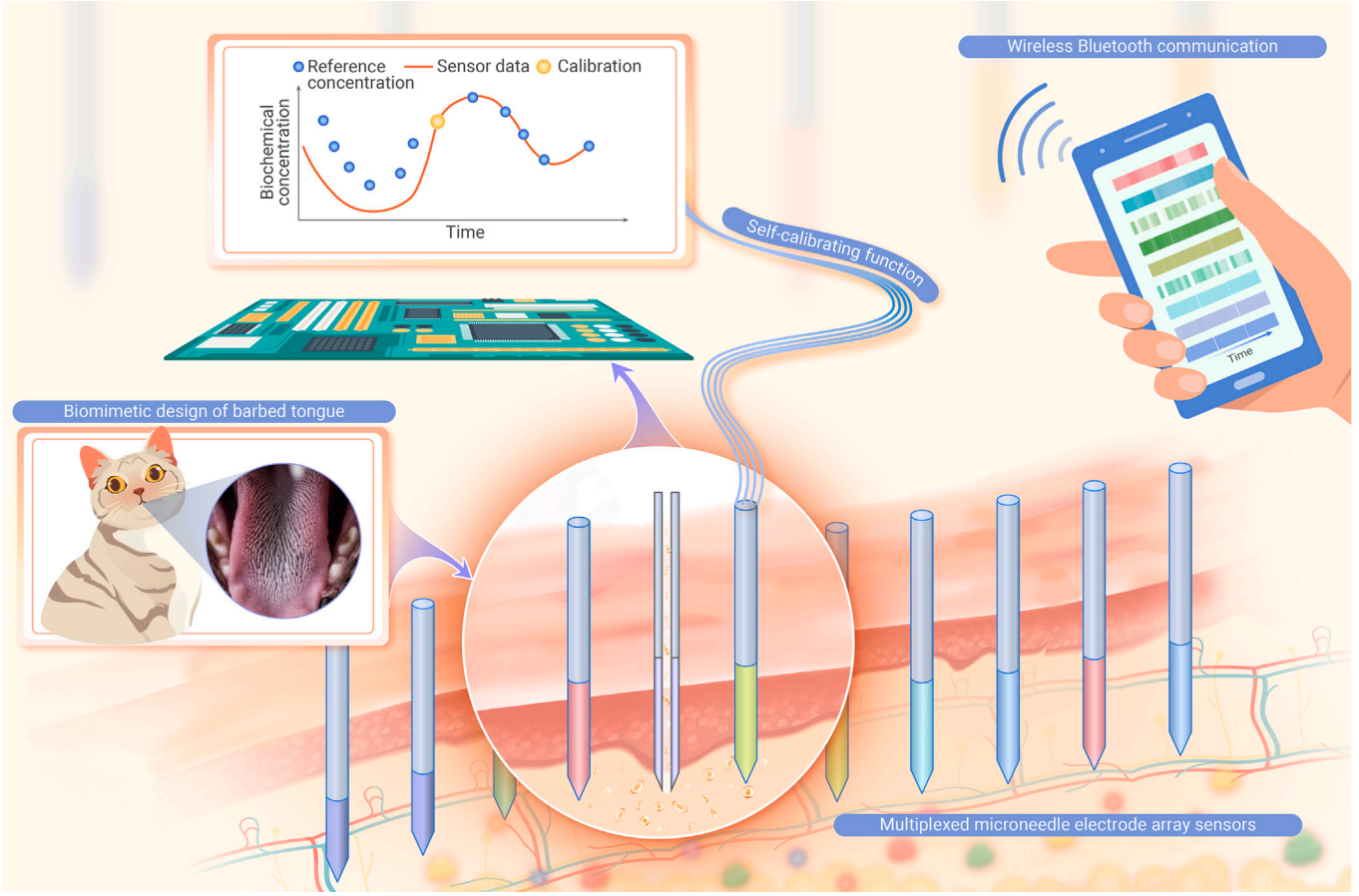

PUBLIC SUMMARY

- The discrete microneedle (MN) electrodes could be freely paired and spliced with a variety of parameters for bio-analysts.
- The discrete MN array facilitating real-time monitoring of complex diabetic states.
- The MN electrode selectively measures glucose, cholesterol, uric acid, lactate, ROSs, Na^+, K^+, Ca^{2+}, and pH.
- The MN self-calibration module could correct the signals *in vivo*.
- The MN self-calibration without the need for invasive blood sampling for calibration.

OPEN ACCESS

REPORT

The Innovation

Self-calibrating multiplexed microneedle electrode array for continuous mapping of subcutaneous multi-analytes in diabetes

Xiangling Li,[1,2,*] Shantao Zheng,[1] Mengyi He,[1] Xinshuo Huang,[1] Cheng Yang,[1] Jingshan Mo,[1] Jingbo Yang,[2] Chengduan Yang,[1] Huijiuan Chen,[1] and Xi Xie[1,2,*]

[1]State Key Laboratory of Optoelectronic Materials and Technologies, Guangdong Province Key Laboratory of Display Material and Technology, School of Electronics and Information Technology, Sun Yat-Sen University, Guangzhou 510006, China

[2]School of Biomedical Engineering, Sun Yat-Sen University, Shenzhen 518107, China

*Correspondence: lixiangling05@outlook.com (X.L.); xiexi27@mail.sysu.edu.cn (X.X.)

Received: May 3, 2024; Accepted: December 26, 2024; Published Online: January 25, 2025; https://doi.org/10.1016/j.xinn.2024.100781

Citation: Li X., Zheng S., He M., et al., (2025). Self-calibrating multiplexed microneedle electrode array for continuous mapping of subcutaneous multi-analytes in diabetes. The Innovation **6(2)**, 100781.

Monitoring multiplexed biochemical markers is beneficial for the comprehensive evaluation of diabetes-associated complications. Techniques for multiplexed analyses in interstitial fluids have often been restricted by the difficulties of electrode materials in accurately detecting chemicals in complex subcutaneous spaces. In particular, the signal stability of enzyme-based sensing electrodes often inevitably decreases due to enzyme degradation or interference *in vivo*. In this study, we developed a self-calibrating multiplexed microneedle (MN) electrode array (SC-MMNEA) capable of continuous, real-time monitoring of multiple types of bioanalytes (glucose, cholesterol, uric acid, lactate, reactive oxygen species [ROSs], Na^+, K^+, Ca^{2+}, and pH) in the subcutaneous space. Each type of analyte was detected by a discrete MN electrode assembled in an integrated array with single-MN resolution. Moreover, this device utilized an MN-delivery-mediated self-calibration technique to address the inherent problem of decreased accuracy of implantable electrodes caused by long-term tissue variation and enzyme degradation, and this technique might increase the reliability of the MN sensors. Our results indicated that SC-MMNEA could provide real-time monitoring of multiplexed analyte concentrations in a rat model with good accuracy, especially after self-calibration. SC-MMNEA has the advantages of *in situ* and minimally invasive monitoring of physiological states and the potential to promote wearable devices for long-term monitoring of chemical species *in vivo*.

INTRODUCTION

Diabetes mellitus is a typical chronic disease that has a large impact on the population and seriously affects human health.[1-5] Continuous glucose monitoring (CGM) technology based on implantable electrodes to measure glucose concentrations in interstitial fluid (ISF) has received US Food and Drug Administration (FDA) approval for diabetes management and commercial applications.[6-8] However, CGM with a longer electrode could be accompanied by adverse reactions, such as concomitant pain, infections, and tissue inflammation.[9-11] Researchers have recently developed microneedle (MN) devices with needle lengths ranging from several hundred micrometers, which are sufficient to penetrate the stratum corneum without reaching the blood vessels or nerves inside the dermis.[12-17] Compared with implantable electrodes of longer size, MNs provide the advantages of being painless and possessing the ability to detect multiplexed analytes through the array structure.[18-20] Compared with noninvasive sensing techniques, MN electrodes can detect more direct and accurate biochemical information in the ISF by bypassing the stratum corneum of the skin.[21-26]

Recent research in the clinical setting has indicated that monitoring multiplexed biochemical markers is beneficial for the comprehensive evaluation of diabetes. The dysregulation of glucose homeostasis leads to variations in the concentrations of electrolytes (ions such as Na^+, K^+, and Ca^{2+}) and may affect acid-base homeostasis in the body.[27,28] In addition, metabolic indicators such as uric acid, cholesterol, lactate, and reactive oxygen species (ROSs) are related to diabetes and have different manifestations with diabetic complications.[29-32] For example, higher uric acid concentrations may indicate type 1 diabetes complicated with nephropathy and may increase the probability of type 2 diabetes.[33-35] Although noninvasive monitoring technologies based on detection in sweat or tears have been proposed, the metabolic components in these biological fluids are susceptible to environmental and other factors, and they rarely reflect the true state of the analytes in the patients' subcutaneous fluid or blood.[36-38] A monitoring technique that can provide real-time *in situ* responses to the concentrations of subcutaneous bioanalytes in a multiplexed manner is still lacking.[39] This challenge is due mainly to delicate sensor fabrication for minimally invasive penetration and difficulties in accurately detecting chemicals in the complex subcutaneous environment.[40]

Electrochemical sensing technology is widely used for the detection of various biochemical indicators because of its advantages of rich detection species, high sensitivity, high selectivity, and easy integration with wearable devices.[41-43] In particular, the combination of MNs and electrochemical sensing technology has the potential to address the disadvantages of destructive and invasive sampling while enabling direct sensing of biochemical information under the skin in a safe and effective way.[44,45] For example, Wang et al. recently reported an integrated wearable device with multiple MN array patches that provided minimally invasive monitoring of glucose-lactate or glucose-ethanol in ISF. The MN electrode patches, which are based on different types of enzyme functionalization, are separated to resolve the electrochemical crosstalk arising from different channels.[46] On the other hand, recent studies have shown that coating nanomaterials on electrochemical electrodes provides unique advantages, such as a larger specific surface area. The nanoscale features, which are similar in size to those of the enzyme, provide close access to the redox center of the enzyme, potentially enhancing the efficiency of enzyme-catalyzing glucose reactions.[47,48] However, during long-term subcutaneous monitoring, the signal stability of enzyme-based sensing electrodes inevitably decreases because of enzyme degradation or interference from the complex biological environment *in vivo*. For commercial CGM, this issue is often ameliorated by invasive calibration by measuring blood glucose levels via blood from fingertips, which increases the risk of pain and infection.[49,50]

In this work, we developed a self-calibrating multiplexed MN electrode array (SC-MMNEA) capable of continuous and real-time monitoring of multiple types of bioanalytes (glucose, cholesterol, uric acid, lactate, ROSs, Na^+, K^+, Ca^{2+}, and pH) in the subcutaneous space. Each type of analyte was detected by a discrete MN electrode assembled in the integrated array. The assembling strategy of fabricating a multiplexed MN sensor array allowed the sensing of analytes with single-MN resolution. This design effectively solved the crosstalk problem associated with direct chemical modification of the MN patch. The hybrid nanostructure of the carbon nanotubes (CNTs) and conductive polymers coated on the MN electrode enhanced the sensitivity and linear range of the MN sensors while maintaining material stability. Moreover, this device utilized an MN-delivery-mediated self-calibration technique to address the inherent problem of decreased accuracy of implantable electrodes caused by long-term tissue variation and enzyme degradation, enhancing the reliability of the MN sensors. The performance of SC-MMNEA was demonstrated *in vivo* in a rat model, and the results indicated that SC-MMNEA could provide real-time monitoring of multiplexed analyte concentrations with good accuracy, especially after self-calibration. SC-MMNEA has the advantages of *in situ* and minimally invasive monitoring of health states and the potential to facilitate wearable diagnostic devices for long-term monitoring of chemical species *in vivo*.

MATERIALS AND METHODS

Preparation of conductive sensing MNs

Acupuncture needles with a diameter of 250 μm and a length of 4.5 cm were used (Flux JS-807, Guangdong Jianxin Technology), polished for 10 min, then cleaned with deionized water and dried. Afterward, they were connected to electrical wires and placed in a gold sulfite plating solution. A current of 0.6 mA was then applied for 15 s, followed by a −0.6-mA

current for another 15 s using an electrochemical workstation (CHI760E, Shanghai CHENHUA) to remove the impurities remaining on the surface of the MNs. The Au layer was deposited on the needle after a 10-min electroplating reaction at a current of −2 mA. Finally, the long needles were cut into short needles and used as Au-plated needle electrodes, referred to as Au MNs. For the preparation of hollow MNs, a Beltran German-quality disposable insulin syringe with a needle (U40) was used for processing. For insulation and tip exposure of the conductive sensing MNs, the Au-plated needles were inserted into polydimethylsiloxane (PDMS; SYLGARD 184, Dow Corning), a PDMS substrate at a controlled penetration depth, and the nonsensing area of the needles was deposited with parylene C via a chemical vapor deposition (CVD) process by Penta Technology (Suzhou).

Preparation of polyimide flexible circuits

Patterns of polyimide (PI) flexible circuits were designed, and fabrication processes such as Cu film deposition, Au electrodeposition, photolithography, etching, and laser cutting were performed (Shenzhen Gaoyue Electronics, Shenzhen, China). First, a Cu film was prepared on the surface of a PI substrate (12.5 μm Kapton film, DuPont) through a deposition process of Cu sputtering and electrodeposition. The Cu films were then formed via photolithography and development processes to strip off nontargeted Cu regions and expose the circuit patterns. To improve biocompatibility, an Au layer was electroplated on the Cu surface. Finally, PI insulation was used to insulate the Cu/Au leads, and the electrode regions were exposed by laser cutting. The PI substrate was cut by a laser according to the designed structure. The holes were drilled to correspond to the size and spacing of the discrete MN electrodes in the MN array.

Preparation of the Au/CNT/Pt MN electrode

The Au-plated needle electrode was dip coated in a dispersion slurry of CNTs (8 wt %, isopropanol-based CNT conductive paste purchased from Nanjing Xianfeng Nanomaterials Science and Technology) three times. The mixture was then placed in an oven at 60°C overnight, which produced the CNT/Au-MN electrode. Next, using an electrochemical workstation (CHI760E, Shanghai CHENHUA), the Au/CNT MN electrode was placed in a Pt plating solution consisting of chloroplatinic acid (8 mM H_2PtCl_6 and 50 mM HCl). Pt nanoparticles were deposited onto the Au/CNT MN electrode after 200 s of electroplating at a current of −2 mA to prepare the Au/CNT/Pt MN electrode.

Preparation of the Au/CNT/PEDOT:PSS/Pt MN electrode

The Au/CNT MN electrode was immersed in 10 mL of a mixed solution of 0.01 M ethylene dioxythiophene monomer (EDOT) and 0.1 M sodium polystyrene sulfonate (NaPSS), and a constant current of 140 μA was applied to the electrode for 400 s. The Au/CNT MN electrode was plated with a Poly(3,4-ethylenedioxythiophene) (PEDOT):polystyrene sulfonate (PSS) coating, namely the Au/CNT/PEDOT:PSS MN electrode. After being washed and lightly blown dry at room temperature, the Au/CNT/PEDOT:PSS MN electrode was connected to a Pt plating solution containing platinum chloroplatinate for electroplating via an electrochemical workstation to prepare the Au/CNT/PEDOT:PSS/Pt MN electrode. Pt nanoparticles were deposited on the electrode after a plating reaction of 200 s at a current of −2 mA.

Preparation of the MN counter electrode and MN reference electrode

Au/Pt MN electrodes were prepared by electrodeposition of Pt layers onto Au-plated MN electrodes at a current of −2 mA for 1,000 s in an electroplating reaction. Au/Ag/AgCl MN reference electrodes were prepared by dip coating the Au-plated MN electrode in a Ag/AgCl slurry (Ag/AgCl conductive ink; ALS) to prepare an Ag/AgCl layer directly on the electrodes. The electrode was then heated in an oven at 90°C overnight. For the preparation of the Au/Ag/AgCl/poly(vinyl butyral) (PVB) MN reference electrode, 79.1 mg of PVB and 50 mg of NaCl were dissolved in 1 mL of methanol. Then, the Au/Ag/AgCl MN reference electrode was submerged in the above solution for 3 h and then removed. The mixture was then heated at 90°C for 60 min.

Preparation of H_2O_2-, glucose-, cholesterol-, uric acid-, and lactic acid-sensing MN electrodes

The Au/CNT/PEDOT:PSS MN electrode was directly used as the sensing electrode for the detection of H_2O_2. Further modification of the Au/CNT/PEDOT:PSS/Pt electrode with a specific enzyme layer could allow the detection of glucose, cholesterol, uric acid, or lactic acid. All chemicals were obtained from Sigma Aldrich. For the glucose electrode, glucose oxidase (50 mg mL^{-1}, Shanghai Aladdin Reagent), bovine serum albumin (80 mg mL^{-1}, Sigma-Aldrich), and glutaraldehyde (2.5 wt % PBS, Shanghai Aladdin Reagent, Shanghai) were dissolved in PBS. These solutions were mixed in a 1:5:2 volume ratio. The Au/CNT/PEDOT:PSS/Pt MN electrodes were dip coated three times in 200 μL of the above glucose oxidase precursor solution via the lift method, dried overnight, and then immersed in Nafion solution (0.2 wt % dissolved in PBS) the next day. The Au/CNT/PEDOT:PSS/Pt/GOx MN electrode was obtained after drying for 12 h at room temperature. For cholesterol electrodes, cholesterol oxidase (25 mg mL^{-1}, Aladdin Reagent Shanghai), bovine serum albumin (80 mg mL^{-1}, Sigma-Aldrich), and glutaraldehyde (2.5 wt % PBS, Aladdin Reagent Shanghai, Shanghai, China) were dissolved in PBS, and the above solutions were mixed at a ratio of 1:5:2. Using an Au/CNT/PEDOT:PSS/Pt MN electrode, the electrode was lifted three times in 200 μL of cholesterol oxidase precursor solution as described above, dip coated three times, dried overnight, and then immersed in Nafion solution (0.2 wt % dissolved in PBS) the next day. The Au/CNT/PEDOT:PSS/Pt/COx MN electrodes were obtained after drying for 8 h at room temperature. For the uric acid electrode, uric acid oxidase (15 mg mL^{-1}, Shanghai Aladdin Reagent), bovine serum albumin (80 mg mL^{-1}, Sigma-Aldrich), and glutaraldehyde (2.5 wt % PBS, Shanghai Aladdin Reagent, Shanghai) were dissolved in PBS, and the above solutions were mixed at a ratio of 1:5:2. Next, the Au/CNT/PEDOT:PSS/Pt MN electrode was dip coated three times in 200 μL of the above uric acid oxidase precursor solution via the lift method, dried overnight, and then immersed in Nafion solution (0.2 wt % dissolved in PBS) the next day. The Au/CNT/PEDOT:PSS/Pt/Uricase MN electrodes were prepared after drying for 12 h at room temperature. For the lactate electrodes, lactate oxidase (30 mg mL^{-1}, Aladdin Reagent Shanghai, China), bovine serum albumin (80 mg mL^{-1}, Sigma-Aldrich), and glutaraldehyde (2.5 wt % PBS, Aladdin Reagent Shanghai, China, Shanghai) were dissolved in PBS, and the above solutions were mixed at a ratio of 1:5:2. Using an Au/CNT/PEDOT:PSS/Pt MN electrode, the electrode was dip coated three times in 200 μL of lactate oxidase precursor solution as described above, dried overnight, and then immersed in Nafion solution (0.2 wt % dissolved in PBS) the next day. The Au/CNT/PEDOT:PSS/Pt/LOD MN electrodes were obtained by drying for 8 h at room temperature.

Preparation of Na^+-, K^+-, Ca^{2+}-, and pH-sensing MN electrodes

Typically, a cocktail of an Na^+-selective membrane was prepared consisting of Na ionophore X (1% weight by weight, w/w, Sigma-Aldrich), Na-TFPB (0.55% w/w, Sigma-Aldrich), poly(vinyl chloride) (PVC, 33% w/w), and DOS (65.45% w/w). Two hundred milligrams of the cocktail was dissolved in 1,320 μL of tetrahydrofuran with shaking on a shaker for 30 min. For the K^+-selective membrane, the cocktail was composed of valinomycin (2% w/w, Sigma-Aldrich), NaTPB (0.5%, Sigma-Aldrich), PVC (32.7% w/w, Sigma-Aldrich), and bis(2-ethylehexyl) sebacate (DOS) (64.7% w/w, Sigma-Aldrich). Two hundred milligrams of the cocktail was dissolved in 700 μL of cyclohexanone to obtain a membrane solution. The cocktail of the Ca2+-selective membrane consisted of a calcium ionophore (ETH 129, 0.46% w/w, Sigma-Aldrich), NaTPB (0.48% w/w, Sigma-Aldrich), PVC (33.02% w/w, Sigma-Aldrich), and 1-nitro-2-(n-octyloxy)benzene (NPOE, 66.04% w/w, Sigma-Aldrich), which was prepared by dissolving 200 mg of cocktail in 1 mL of tetrahydrofuran. All the ion-selective solutions were sealed and stored at 4°C when not used. Ion-selective membranes were then prepared by dip coating the corresponding electrodes with an Na^+-, K^+-, and Ca^{2+}-selective membrane cocktail. The electrodes were allowed to dry overnight in an ambient environment. The pH-sensing coating was prepared by dissolving 20 mg of polyaniline emeraldine in 20 mL of dimethyl sulfoxide (DMSO, Sigma-Aldrich). To ensure complete dissolution, the mixture was stirred for 24 h. The MN electrodes were dip coated with a polyaniline emeraldine solution and dried for 2 h at 80°C to prepare a polyaniline emeraldine base membrane on the Au electrode. The membrane was then incubated with 2 mL of HCl solution (1 mol/L, Sigma-Aldrich) in a vacuum chamber for 5 h.

Device integration

After the flexible circuit board was obtained, the MN array connector was prepared. A retractable, spring-loaded thimble was embedded in each aperture of the flexible circuit board. These thimbles were then soldered to the pads surrounding the apertures using solder to form a solid connection between the thimbles and the circuit board. This completed the preparation of the MN array connector. The arrayed, spring-loaded thimbles in the connector could be pressed down under stress, contacting the sensing electrodes in the MN array, thus realizing a precise connection between the connector and the MN array. Additionally, the alignment of the flexible circuit board was extended backward by a certain length from the aperture, and a flexible printed circuit (FPC) interface was formed at the end of the board. Through the FPC interface, the MN array connector was connected to the detection circuit, enabling signal transmission from the MN array to the monitoring system. The preparation of the MN arrays involved combining discrete MN electrode components and embedding them into the grooves of a resin substrate. In this project, the MN array substrate was prepared via three-dimensional (3D) printing technology. This method effectively controls the cost and process complexity of MN array preparation, enabling efficient production.

After the functionalization and modification were completed, the long shanks of the MN electrodes were cut off, retaining only the solder joint portion to form the final, discrete MN

electrode components. The solder joint on the MN electrode served as the contact point between the MN array connector and the electrode itself. By combining MN electrodes with different functionalities, MN arrays of various specifications can be efficiently prepared. Moreover, any discrete MN electrode within the array could be quickly replaced if necessary. To assemble the MN array detection system, the arranged MN electrode components were embedded into the grooves of the MN array substrate. Under pressure, the arrayed spring thimbles of the MN array connector made a precise connection with the MN electrodes, simultaneously securing them in place. Additionally, the FPC interface at the end of the connector was connected to the hardware detection circuit, establishing the signaling pathway between the MN arrays and the detection circuits. The length of the needle electrodes could be adjusted by varying the thickness of the substrate, ensuring that the depth of insertion into the subcutis was maintained at the micrometer level (within 1,000 μm).

Surface morphology characterization and elemental analysis of the sensing electrodes

The surface morphology of the sensing electrodes and calibration electrodes at different stages of modification was imaged via a benchtop scanning electron microscope (Phenom Pro, Phenom Scientific Instruments). To characterize the sensing electrodes after material modification from a cross-sectional view, the surface of the core electrode and the material morphology were observed via field emission SEM (FE-SEM, SUPRA 60, Zeiss). Moreover, the material element contents of the Au/CNT/PEDOT:PSS/Pt MN electrodes were analyzed via the EDX module in the FE-SEM system. The material elemental ratios were further analyzed. The Au/CNT/PEDOT:PSS/Pt MN arrays were characterized via benchtop SEM with a camera system. X-ray photoelectron spectroscopy (XPS) is commonly used to analyze the elemental composition and compound valence of materials. High-resolution transmission electron microscopy (HRTEM) was used to analyze the elemental composition of the materials. Transmission electron microscopy (TEM) images were obtained via a transmission electron microscope (FEI Tecnai G2 F30). X-ray diffraction (XRD) was used to analyze the crystal structure of the material via an XRD instrument (Rigaku SmartLab 9k).

Electrochemical characterization of the sensing electrodes

The MN electrode (working electrode) used for the biochemical assays was characterized via an electrochemical workstation (CHI760E, CH Instruments). The selectivity of the MN electrodes for glucose, cholesterol, lactate, uric acid, ROSs, Na^+ ions, K^+ ions, Ca^{2+} ions, and pH sensing was evaluated separately by sequentially adding certain concentrations of interfering substances to the solution. For the MN ion electrodes, the electrochemical workstation characterized the open-circuit potential of the two-electrode system, where a commercial Ag/AgCl electrode was used as a reference electrode during the test. The open-circuit potential was recorded for different concentrations of the substance to be measured. A series of ion solutions with different concentrations were prepared, in which deionized water was used as the solvent. The test was paused for 30 s each time the concentration of the substance changed to allow for sufficient mass transfer in the solution. Interference studies were carried out by adding 2 mM uric acid, 2 mM cholesterol, 2 mM lactic acid, 0.5 mM vitamin C, 10 mM NaCl, 0.5 mM $CaCl_2$, 5 mM $MgCl_2$, or 2 mM KCl dissolved in deionized water. For the MN electrodes for metabolite sensing, a three-electrode system (working, counter, and reference electrodes) was used, where the amperometric sensors applied bias potentials of 0.35, 0.45, −0.35, 0.4, and −0.1 V when the specified bias potentials were applied for the sensing of glucose, cholesterol, lactate, uric acid, and H_2O_2, respectively. A commercial Pt electrode was used as the counter electrode, and a commercial Ag/AgCl electrode was used as the reference electrode during the test to provide a better reference for the MN working electrode during the *in vitro* experiments. Notably, cholesterol has a low solubility in PBS, and 15% trilatone (Triton X-45, Sigma-Aldrich) was used as a dispersant, where the ratio of trilatone:PBS was 1:3 (v/v). Interference studies were performed by adding 2 mM glucose, 50 μM uric acid, 10 μM vitamin C, 2 mM lactic acid, or 10 mM KCl. The effect of the material on the sensing performance was assessed by measuring the electrochemical properties of MN electrodes with different material structures. The sensitivity, detection selectivity, and detection range of each electrode were analyzed separately, and the results were normalized and compared.

Simulation of the MN-mediated self-calibration technique

COMSOL Multiphysics 5.5 was used to perform the theoretical simulations. The simulation uses a simplified 3D model (16 × 16 × 10 mm with open boundaries) with geometry and components that mimic the actual setup. Two MNs are used as representative, where one solid MN represents the sensing electrode and the other one is a hollow MN (solid MN with the open hole facing the right side) that represents the calibration electrode. The inner diameter of the hollow MNs was 0.15 mm, the interval between two neighboring needles was 3 mm, and the transdermal depth of the MNs was 0.8 mm. The thicknesses of the different skin layers were 0.02 mm (stratum corneum), 0.2 mm (active layer), and 2 mm (dermis). The initial concentration of glucose was set to C0, and the top boundary of the hollow channel of the MN was set as the inflow boundary for a constant drug concentration (C0) to simulate the continuous replenishment of standard glucose molecules. It was assumed that the glucose molecules could further diffuse into any region of the subcutaneous tissue, so the boundary around the tissue in the model was set to be open. Under the action of a constant-flow pump, glucose continuously diffuses through the hollow microchannel of the MN at a constant flow rate V0 into the subdermal tissue, and the direction of the fluid is oriented toward the end of the MN-sensing electrode. The concentration of glucose detected by the MN electrode was obtained by calculating the concentration of glucose accumulated in the average area of the MNs under the dermis. The relevant physical parameters for the simulation were as follows: Dg, Dsc, and Dde represent the relative molecular diffusion coefficients of glucose in aqueous solution, the stratum corneum, and the dermis, respectively. Vw and Vde represent the kinetic viscosity of the aqueous solution and dermis, respectively. C0 was the initial concentration of glucose. V0 was the initial glucose inflow velocity. These detailed parameters related to the physical setup can be found in the attached table of the supplemental information. The dilute substance transfer interface was used through the chemical substance transfer module to simulate the dynamic transport process of the studied chemical components, and the substance satisfied the mass conservation Equation 1:

$$\frac{\partial c_i}{\partial t} + \nabla \cdot J_i + u \cdot \nabla c_i = R_i \quad \text{(Equation 1)}$$

This equation includes the transport mechanisms of diffusion and convection, where ci is the concentration of the substance, ∇ is the Hamiltonian operator, R_i is the expression for the rate of reaction of the substance, and u is the mass-averaged velocity vector. Diffusion of molecules often induces mass transport at dilute substance transfer interfaces, in which case the mass flux Ji defines the diffusive flux vector, and J_i is associated with the conservation of mass Equation 1 for calculating boundary conditions and fluxes, where D_i is the diffusion coefficient.

$$J_i = -D_i \nabla c_i \quad \text{(Equation 2)}$$

The laminar flow interface was invoked through the fluid flow module to be used for calculating the velocity and pressure fields of the drug flow in the laminar state. The equations solved for the laminar flow interface are based on the Navier-Stokes equations, which have the following general form:

$$\rho \frac{\partial u}{\partial t} + \rho(u \cdot \nabla)u = \nabla \cdot [-pI + k] + F \quad \text{(Equation 3)}$$

$$\rho \nabla \cdot u = 0 \quad \text{(Equation 4)}$$

where Equation 3 is a vector equation representing the conservation of momentum and Equation 4 is a continuity equation representing the conservation of mass. ρ denotes the density, u denotes the velocity vector, p represents the pressure, k represents the viscous stress tension, and F represents the volumetric force vector.

In vitro self-calibration experiments

A solid MN glucose electrode was employed as the sensing electrode, whereas an adjacent hollow MN serving as the delivery electrode was utilized as the calibration electrode, both of which were inserted into the solution. The solid MN glucose electrode was inserted to a full immersion depth of 1.2 mm and partially inserted to a depth of 0.6 mm into the solution. For each insertion depth, the MN electrodes detected current signals corresponding to a series of glucose concentrations (0, 5, and 10 mM), yielding respective signal–concentration curves. The solid MN glucose electrode, inserted at a depth of 0.6 mm, was continuously monitored in a 2 mM glucose/PBS solution for 600 s followed by the introduction of calibration solutions at concentrations of 5, 10, and 20 mM at the 100-s time point, which were administered through the hollow microchannel at a constant flow rate of 0.3 mL/min via peristaltic pumping. The entire process was recorded as i-t curves. The maximum current values attained at 100 s post injection were denoted as Imaxg1, Imaxg2, and Imaxg3. The obtained current-concentration relationship facilitated recalibration and determination of the calibrated concentration of the original solution. The external calibration of cholesterol followed a similar procedure for glucose sensing. The MN electrode for cholesterol sensing, alongside an adjacent hollow MN, was inserted into the cholesterol solution, with immersion depths of 1.2 mm for full insertion and 0.6 mm for partial insertion into the solution. Current signals corresponding to a series of cholesterol concentrations were detected for each insertion depth, generating respective signal-concentration curves. The solid MN cholesterol electrode, which was subsequently inserted at a depth of 0.6 mm, was continuously monitored in a 2 mM cholesterol/PBS solution for 600 s, followed

by the introduction of calibration solutions at concentrations of 5 and 10 mM at the 100-s time point and administration through the hollow microchannel at a constant flow rate of 0.3 mL/min. The entire process was recorded as i-t curves. The maximum current values attained at 100 s post injection were denoted as Imaxc1 and Imaxc2, facilitating calibration completion.

Printed Circuit Board (PCB) design

The two-electrode system for Na^+, K^+, Ca^{2+}, and pH sensing can record signals associated with the ion concentration by outputting different open-circuit voltages. To achieve this function, a differential amplifier module with high input impedance and low output impedance was used for signal amplification and reduction of common mode interference. On the other hand, the three-electrode system includes glucose, cholesterol, lactate, uric acid, and H_2O_2 electrodes to detect the glucose concentration in the ISF via the amperometric method. Precision opamps with low input bias current, low output voltage, and low output voltage temperature drift were used as voltage followers and transimpedance amplifiers to meet the requirements of constant potential circuits. The voltage between the reference electrode and working electrode was kept stable by maintaining the reverse potential of the counter electrode to improve the accuracy of the glucose sensor in detecting the corresponding current. The microcontroller unit (MCU) was centered on an STM32F103C8T6 microcontroller (ARM 32-bit), which can be programmed onboard through a serial line debugging interface. In this unit, an analog-to-digital converter was used to detect the amplified signal from the SC-MMNEA sensor, whereas a Digital-to-Analog Converter (DAC) provided a suitable reference voltage for the constant potential module. Control inputs/outputs (I/Os) allow control of the flow rate of the peristaltic micropump and the switching of the pressurizing element. Additionally, communication with a computer or a Bluetooth module (low-power Bluetooth chip CC2640R2F) could be realized via a serial port.

Animal experiments

Male Sprague-Dawley (SD) rats weighing 220–250 g and approximately 8 weeks old (Animal Center of Sun Yat-sen University, Guangzhou, China) were used for the experiments. The rats were housed in a climate-controlled room with a 12-h light/12-h dark cycle and provided with food and water. Type 1 diabetic rats were induced with streptozotocin (Sigma-Aldrich) at a dose of 60 mg/kg. The BGL of these strains was detected for at least 7 days. Rats in which the blood glucose level stabilized above 300 mg/dL were successfully induced.

Application of the MN sensor to rats

The Sprague-Dawley rats were anesthetized using an anesthesia system (C90, RIDTER, Beijing, China) with 2% isoflurane gas delivered via a nose cone. Prior to experimentation, the dorsal fur of the rats was removed using depilatory cream (VEET Depilatory Cream, Reckitt Benckiser). The MN array was subsequently inserted through the skin layer of the rats and fixed onto their backs for detection purposes. The 4 × 4 integrated MN sensor array was divided into four separate arrays of 4 MN electrodes each, all of which were simultaneously affixed to the dorsal skin of the rats. The multiparameter MN electrode array detected and recorded the ISF levels of glucose, lactate, uric acid, cholesterol, ROS (H_2O_2), Na^+, K^+, Ca^{2+}, and pH every 30 min. Concurrently with the MN data recording, tail blood samples were collected from the rats, and the values of nine biochemical indicators in the blood were determined via a commercial biochemical analyzer (Clinical Chemistry Analyzer BS-240, Mindray). The sensing sessions lasted for 4 h each day, spanning a total of 3 days. At the end of each daily experiment, the rats were allowed to recover from the anesthetized state, and the MN array was withdrawn to allow the rats to return to the cage after each set of experiments. The MN array was reapplied to the rat for the sensing experiment the next day. Additionally, during each experimental day, healthy rats were intraperitoneally injected with a glucose solution during the first 1.5 h to induce fluctuations in internal glucose levels. Conversely, diabetic rats induced with streptozotocin were subcutaneously injected with insulin solution during the same time frame. To calculate the MN-detected electrical signals as metabolite concentrations, the first recorded signal data point was paired with the reference concentration detected via the standard method. To calculate the concentration of MN-detected electrical signals as ions, the first two recorded signal data points were paired with the reference concentration detected via the standard method. The data pair was used to calculate the signals into concentrations. To validate the *in vivo* application of the MN self-calibration technique, at the fourth hour of each experimental day, healthy rats received a 0.1-mL mixture of 10 mM glucose and 4 mM cholesterol solution, whereas diabetic rats received a 0.1-mL mixture of 25 mM glucose and 4 mM cholesterol solution, both of which served as calibration solutions. The current signals of the MN sensors were recorded following the delivery of the calibration solutions.

Statistical analysis

The data were calculated and expressed as the means ± SD. Grid analysis refers to the plotting of commercially referenced concentration values as the abscissa and sensor concentration readings as the ordinate. In this context, glucose grid analysis employs Clark error grid analysis for evaluation. The manuscript addresses various parameters, including glucose, cholesterol, uric acid, lactate, ROSs, Na^+, K^+, Ca^{2+}, and pH. All heat maps presented within the manuscript were derived from converting these parameter values into percentages relative to their maximum concentration values. The error was calculated as the relative discrepancy between sensor readings and commercially referenced values, using the formula for relative error. The assessment of error was determined by averaging the errors across all samples.

Ethical statement and patient consent

The experimental protocols were approved by the Institutional Animal Care and Use Committee of Sun Yat-sen University. All animals were handled following the guidelines for the care and use of laboratory animals described by the Institutional Animal Care and Use Committee of Sun Yat-Sen University (SYSU-IACUC-2021-000022, SYSU-IACUC-2021-000020).

RESULTS AND DISCUSSION

Design and fabrication of SC-MMNEA

In nature, the barbed tongue of felines possesses needle-like spikes on the tongue (Figure 1A). Different types of taste buds can sense different types of flavors (e.g., sweet, sour, bitter, salty, and umami) and are distributed on the tongue surface. To mimic the structure and function of the barbed tongue, we developed a multiparametric MN system capable of simultaneously detecting various indicators, including glucose, cholesterol, uric acid, lactate, ROSs, Na^+, K^+, Ca^{2+}, and pH. This system consists of three components: a multianalyte MN array sensor, a self-calibration module, and an electronic circuit module (Figure 1B). The characteristic feature of the MN sensing module is that each MN can detect a single specific analyte. The number of MNs in the MN array can be flexibly designed, and each MN can be detached or combined as needed. Thus, MN arrays can be designed with specific detection functionalities tailored to requirements. The principle of the self-calibration module involves the use of hollow MNs to deliver a solution of known concentration into the ISF, and an adjacent MN electrochemical electrode rapidly measures the concentration of the target analyte in the local ISF at that moment. Therefore, an accurate relationship is obtained between the electrochemical signal and the known concentration of the target analyte. The standard curve of the current signal-target analyte concentration obtained through this method can further be used to calibrate the electrochemical signals recorded at other times, thereby correcting the measured concentrations of the target analytes. The circuit module supports multiparameter sensing (Figure 1C). SC-MMNEA technology has several main advantages. (1) MN electrodes are less invasive and painless than conventional implanted CGM electrodes. (2) The strategy of assembling discrete MNs into an array solves the crosstalk problem associated with the direct chemical modification of an MN array, resulting in a set of vertically aligned multiplexed MN sensor arrays. (3) Discrete MN electrodes can be freely paired and spliced with a variety of parameters to meet the patient's needs for a wide range of critical bioanalytes. (4) SC-MMNEA enables *in situ* sensing of multiplexed bioanalytes in ISF and selectively measures glucose, cholesterol, uric acid, lactate, ROSs, Na^+, K^+, Ca^{2+}, and pH. (5) SC-MMNEA introduces an MN self-calibration module to correct the signals *in vivo*. This approach effectively solves the inherent problems faced by current CGM devices, which require invasive blood sampling for calibration.

The MN array was fabricated using a hybrid fabrication strategy, including chemical modification, laser micromachining, 3D printing, lithographic micromachining, and weld fixing, to create one-dimensional (1D) functional MN tips for integration. This strategy simplified the complexity of fabricating 3D functional structures. A thin layer of Au was electrodeposited on the surface of the MN electrode to form a Au electrochemical working electrode, which was modified with a corresponding electrochemically sensitive layer to achieve sensing of the target molecule. Chemical vapor deposition of parylene was used to encapsulate the MN electrodes and expose their tips (Figure S1). The functionalization of MN electrode arrays for subcutaneous sensing presents significant challenges. The MN-sensing electrodes in an array were located in a narrow space, where performing functional coating modifications could lead to crosstalk between neighboring electrodes. On the other hand, the small surface area of the MN electrodes limits the detection sensitivity of a single MN tip. To address the challenge

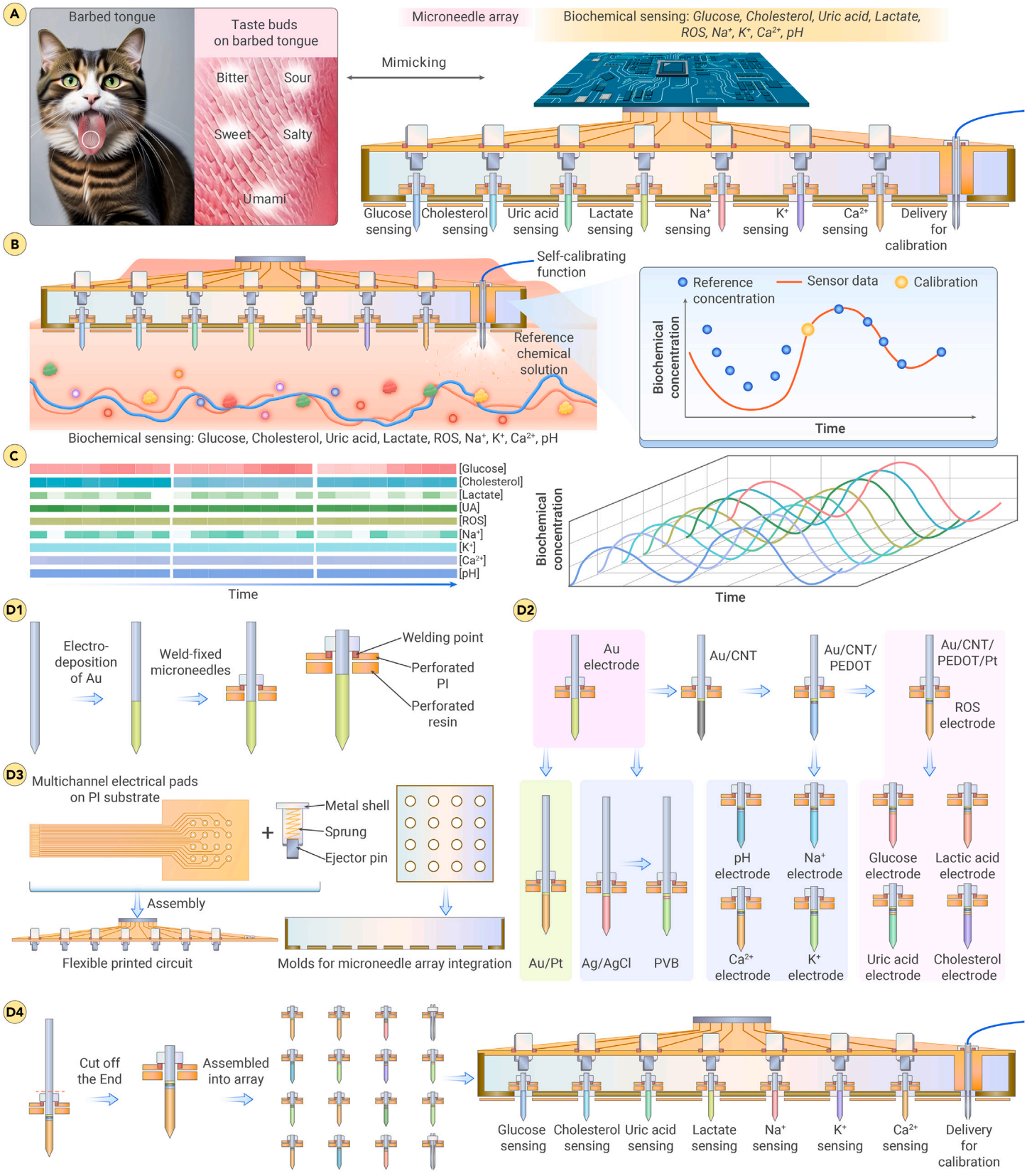

Figure 1. Concept of SC-MMNEA and schematic diagram of MN electrode processing and system integration (A) Schematic diagram of SC-MMNEA mimicking feline tongue barbed sensing. (B) Schematic diagram showing the ability of SC-MMNEA to penetrate the skin in a minimally invasive manner with continuous monitoring of multiple analytes (nine types) with self-calibration functions. (C) Schematic diagram showing the concentration fluctuations of the analytes detected by SC-MMNEA, with continuous monitoring of the concentrations of nine types of bioanalytes in the subcutaneous ISF. (D) Illustration of the SC-MMNEA fabrication process via hybrid fabrication and dimensional reduction and assembly strategies, including (1) fabrication of MN electrodes, (2) MN electrode surface functionalization, (3) microfabrication of circuits and connectors, (4) MN array assembly, and SC-MMNEA system integration.

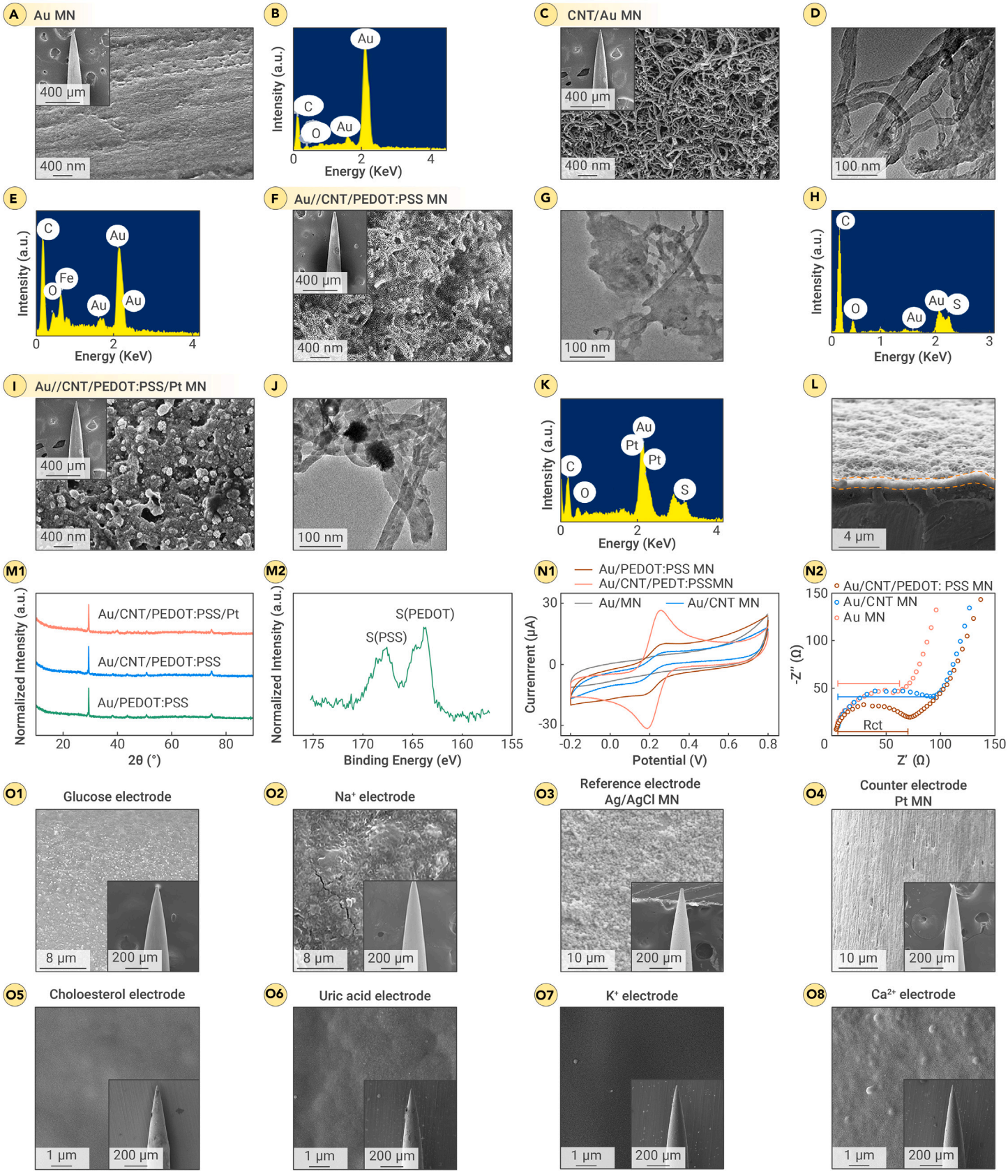

Figure 2. Characterization of the MN of SC-MMNEA (A) SEM image of a stainless-steel electrode plated with Au and a magnified image of the surface morphology. (B) Energy-dispersive X-ray spectroscopy (EDX) of a Au-plated MN electrode. (C) SEM image of a CNT-coated electrode. (D) TEM image of a CNT-coated electrode. (E) EDX of an Au/CNT MN electrode. (F) SEM image of an Au/CNT/PEDOT:PSS MN electrode. (G) TEM image of the Au/CNT/PEDOT:PSS MN electrode. (H) EDX of an Au/CNT/PEDOT:PSS MN electrode. (I) SEM image of the Au/CNT/PEDOT:PSS/Pt MN electrode. (J) TEM image of the Au/CNT/PEDOT:PSS/Pt MN electrode. (K) EDX of the Au/CNT/PEDOT:PSS/Pt MN electrode. (L) SEM image of a cross-section of the Au/CNT/PEDOT:PSS MN electrode. (M) Elemental and compositional analysis of the MN electrode, which included (1) X-ray diffraction (XRD) and (2) X-ray photoelectron spectroscopy (XPS) of the Au/CNT/PEDOT:PSS, Au/CNT/PEDOT:PSS, and Au/CNT/PEDOT:PSS/Pt MN electrodes. (N) Electrochemical activities of the electrodes in

(legend continued on next page)

of mutual crosstalk during the modification of MN-sensing electrodes, we adopted a strategy of dimensional reduction fabrication and discrete assembly to prepare MN-sensing electrodes in arrays (Figure 1D). Specifically, an Au layer was first electrodeposited on steel needle electrodes (~250 μm in diameter). These electrodes were then modified with chemically sensitive substances to enable sensing at the MN electrodes. Recent advances have shown that the sensing performance of electrodes can be improved via the use of nanomaterials for coating.[45] CNTs are 1D carbon nanomaterials that possess excellent electrical conductivity, mechanical durability, and a large specific surface area. In addition to modifying the MN surface with CNTs, we coated a thin layer of PEDOT:PSS on top of the CNTs to form CNT/PEDOT:PSS nanocomposites (Figure S2). The MN electrodes were subsequently modified into corresponding enzyme electrodes, ion electrodes, counter electrodes, and reference electrodes (Figures S3–S5). For the detection of metabolites (glucose, uric acid, lactate, and cholesterol) and ROSs (H_2O_2 as an example) in the enzyme-based electrodes, the amperometric method was used for sensing. For ion sensing, the MN electrodes were functionalized with H^+-, Na^+-, K^+-, and Ca^{2+}-selective membranes. These membranes selectively allow the target ions to migrate, thereby creating a concentration gradient on the electrode surface and generating a potential difference related to the ion concentration. The MN array connector was prepared by designing and preparing a flexible circuit board combined with a spring-loaded thimble. On one end of the MN array connector, the thin array was connected to the MNs, and, on the other end, the FPC interface was connected to the detection circuit. The spring-loaded thimbles arrayed in the connector could be pressed down under stress and contact the sensing electrodes in the MN array, thus achieving a precise connection between the connector and the MN array. Discrete MN electrode components were embedded in the MN array substrate for fixation after combination to prepare the MN array.

The sensing electrodes, counter electrodes, reference electrodes, and hollow calibration electrodes were assembled together into an integrated MN array. Here, free assembly into 4 × 4, 3 × 3, and 2 × 2 MN electrode arrays could be achieved according to the design (Figures 1D–4). In practical applications, the MN array connector is tightly connected to the contact points of discrete MN electrodes under pressure. For example, a 4 × 4 MN array containing 16 MN electrodes contained a set of ion-sensing electrodes, including a pH electrode, a Na^+-ion-sensing electrode, a K^+-ion-sensing electrode, and a Ca^{2+}-ion-sensing electrode. The ion-sensing electrodes used a two-electrode system for electrochemical potentiometric detection and an Ag/AgCl electrode as a reference electrode. The MN electrode array also contained electrodes for ROSs, glucose, lactate, uric acid, and cholesterol sensing. These electrodes use a three-electrode system for electrochemical detection, and the detection of lactate and uric acid involves a reference electrode and a counter electrode. The detection of ROSs, glucose, and cholesterol involved the use of another reference electrode and a counter electrode. In addition, the MN array contained two hollow MNs for self-calibration. Notably, in our device, each MN could be withdrawn or replaced with another type of MN electrode in a flexible way. Therefore, the MN electrodes could be flexibly combined to form a desirable sensor array according to the application purpose. Each MN electrode could be readily replaced with a new electrode if it degraded. In addition, the length of the MN could also be changed by adjusting the thickness of the space layer underneath (Figure S6).

Morphological characterization of the MN electrodes

The structure and surface morphology of the MN electrodes during different preparation processes were characterized by scanning electron microscopy (SEM). After electrodeposition with a Au layer, the native stainless-steel MN electrodes and hollow MNs exhibited a smooth morphology on the coated surface (Figures 2A and S7). Material composition characterization by energy-dispersive X-ray spectroscopy (EDX) confirmed the presence of Au, C, and O on the electrode surface (Figure 2B). After being coated with hybrid CNT nanomaterials, the electrode surface displayed a hybrid micro/nanomorphology with an interconnected dense nanogrid structure (Figure 2C), as shown by both the SEM and TEM (Figure 2D) images. The electrode coated with the CNT nanocomposites was further characterized by EDX. Here, the presence of C and O in the CNT nanocomposites was confirmed (Figure 2E). After PEDOT:PSS electrodeposition, both the SEM and TEM images revealed that the CNTs were encapsulated by a polymer layer (Figures 2F and 2G), whereas PEDOT:PSS bridged the CNT nanonetwork. The CNT/PEDOT:PSS hybrid nanomaterials were further characterized via EDX, and the presence of S, C, and O was confirmed (Figure 2H). After electrodeposition with the Pt nanoparticles, both the SEM and TEM results indicated that the Pt nanoparticles were successfully coated on the surface of the Au/CNT/PEDOT:PSS MN electrode (Figures 2I and 2J). The Pt peaks observed via EDX clearly appeared after electrodeposition, indicating that the electrode surface was loaded with a significant amount of Pt (Figure 2K). The SEM image shows a cross-sectional view of the Au/CNT/PEDOT:PSS/Pt MN electrode surface. The thickness of the nanomaterial layer was ~1.3 μm, and the electrode surface was uniform (Figure 2L). The XRD spectrum of the Au/CNT/PEDOT:PSS/Pt MN electrode is shown in Figure 2M-1, where the specific XRD peaks at 2 Theta values of 42.9°, 67.9°, and approximately 81.8° suggest the presence of PEDOT:PSS.[51] XPS is commonly used to analyze the elemental composition and valence states of material surfaces. The specific peaks of the Au/PEDOT:PSS MN electrodes at approximately 164 and 167 eV represented the characteristic peaks of PEDOT and PSS, respectively (Figures 2M-2 and S8).[52]

Cyclic voltammetry (CV) measurements of the Au/CNT MN, Au-MN, and Au/CNT/PEDOT:PSS MN electrodes were performed in a solution containing 5 mM potassium ferricyanide and 0.1 mM KCl, and the results are shown in Figure 2N-1. The electrochemical performance of the Au/CNT/PEDOT:PSS MN electrode exceeded those of both the Au/PEDOT:PSS MN and the Au/CNT MN electrodes. These results indicated a synergistic increase in the electrocatalytic activity of the Au/CNT/PEDOT:PSS hybridized material. To analyze the electrochemical impedance of the Au/CNT MN, Au-MN, and Au/CNT/PEDOT:PSS MN electrodes in solution, Nyquist impedance spectra were obtained for the above electrodes in the frequency range of 100 kHz–0.01 Hz in a mixed solution of 5 mM potassium ferricyanide and 0.1 mM KCl. Rs was insensitive to the coating components of the electrodes, with a value of approximately 4.2 Ω for all the above coatings. However, the Rct values of the different coatings significantly varied, with Rct = 52.5 Ω for the Au MNs, Rct = 88.6 Ω for the Au/CNT MNs, and Rct = 67.2 Ω for the Au/CNT/PEDOT:PSS MNs (Figures 2N-2, S9A, and S9B). These results occurred because the resistance of the CNTs was greater than that of the Au layer. The CNTs exhibited a fiber-like network structure, where the boundary between different CNTs in contact could hinder electron transfer, resulting in increased resistance. Since the PEDOT:PSS possessed good conductivity and bridged different CNTs, the resistance of the Au/CNT/PEDOT:PSS MNs was lower than that of the Au/CNT MNs. Thus, the resistance of the CNT network was reduced in the Au/CNT/PEDOT:PSS MNs. After coating with Pt, the resistance of the MN electrode decreased. Notably, the Au/CNT/PEDOT:PSS/Pt MN exhibited the lowest Rct value of 42.3 Ω and outperformed its Au/Pt MN counterpart, with Rct = 49.3 Ω (Figure S9C). This reduction in resistance was likely caused by the ability of the Au/CNT/PEDOT:PSS MN surface to facilitate the selective adsorption of Pt nanoparticles, thereby increasing the electron transfer rate and ion diffusion within the electrolyte solution. To assess coating durability during MN implantation in the skin (Figure S2), CNT/Au MNs and Au/CNT/PEDOT:PSS MNs were inserted into pigskin with controlled force, left for 5 min, and then removed. The Au/CNT MNs shed some of the coating during insertion and removal (Figure S10A), whereas the Au/CNT/PEDOT:PSS MNs remained more stable after skin penetration (Figure S10B). Furthermore, the MN electrode with a steel base could even punch into watermelon rinds, demonstrating the good mechanical strength of the steel-based MN electrode compared with other commonly used MN materials, such as polymers and hydrogels (Figure S11).

Furthermore, we characterized the morphology of the functionalized multifunctional MN electrodes. All the functionalized MN electrode surfaces exhibited uniform coating layers (Figure 2O). The MN glucose electrode was modified with glucose oxidase, with the enzyme layer uniformly spread on the electrode surface

the standard redox reaction. (1) CV curves of the Au/CNT MN, Au-MN, and Au/CNT/PEDOT:PSS MN electrodes tested at 100 mV/s scanning. (2) Nyquist impedance spectra of the CNT/Au-MN, Au-MN, and Au/CNT/PEDOT:PSS MN electrodes. (O) Schematic and SEM images showing the structure and surface morphology of the SC-MMNEA, including the (1) MN glucose electrode, (2) MN Na^+ electrode, (3) MN Ag/AgCl reference electrode, (4) MN counter electrode, (5) MN cholesterol electrode, (6) MN uric acid electrode, (7) MN K^+ electrode, and (8) MN Ca^{2+} electrode.

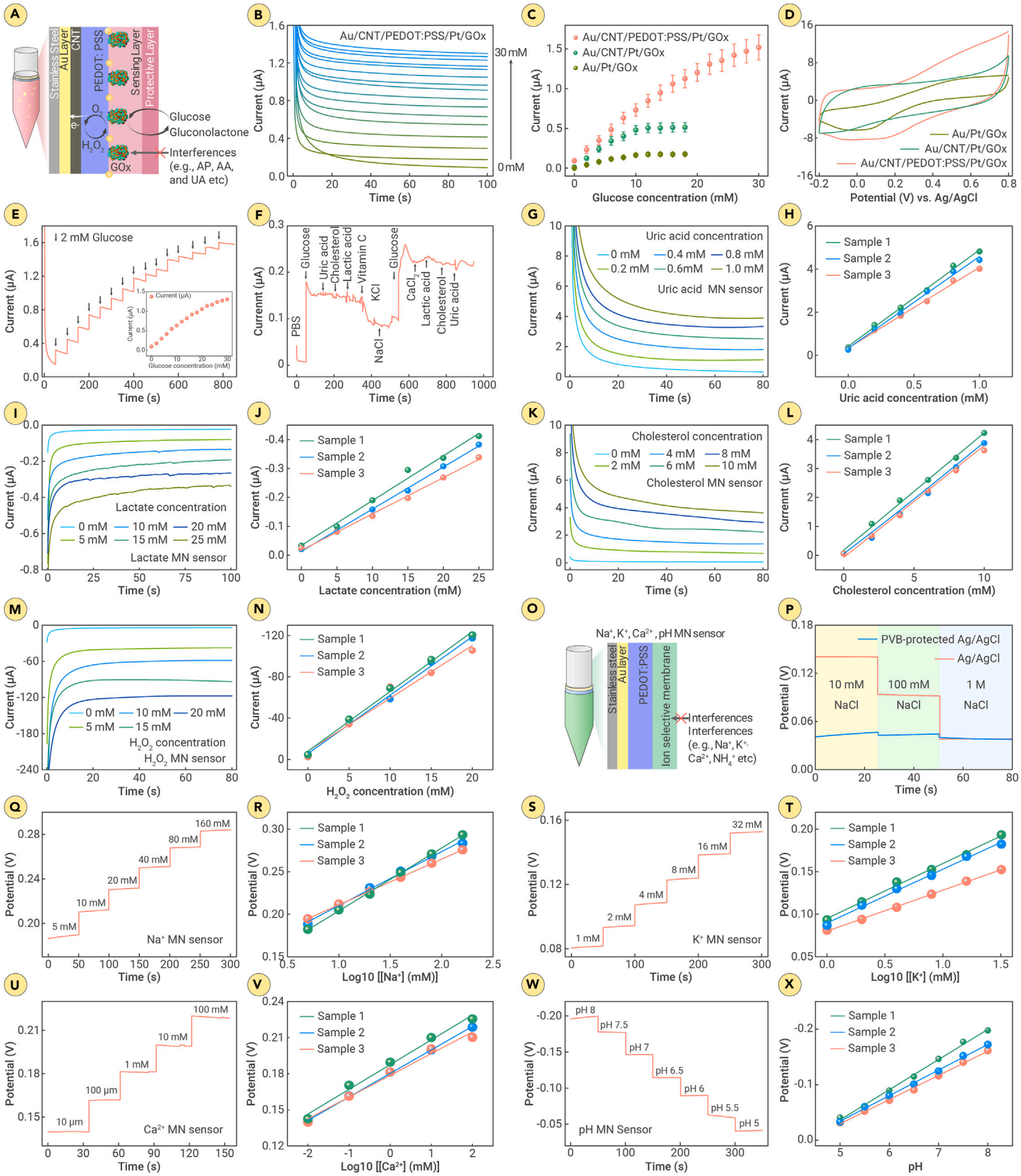

Figure 3. ***In vitro*** **electrochemical performance characterization of the MN electrodes** (A) Schematic of the MN glucose electrode with multiple functional layers. (B) Amperometric response of the Au/CNT/PEDOT:PSS/Pt/GOx MN electrode at glucose concentrations ranging from 0 to 30 mM. (C) Amperometric response of the MN electrodes coated with different material layers, including Au/Pt/GOx MNs, Au/CNT/Pt/GOx MNs, and Au/CNT/PEDOT:PSS/Pt/GOx MNs, upon sensing different glucose concentrations (N = 3 per group). (D) CV curves of the MN electrodes coated with different material layers, including Au/Pt/GOx MNs, Au/CNT/Pt/GOx MNs, and Au/CNT/PEDOT:PSS/Pt/GOx MNs. (E) i-t curves of the Au/CNT/PEDOT:PSS/Pt/GOx MN electrode for glucose sensing. (F) Presence of uric acid, cholesterol, lactic acid, vitamin C, KCl, and NaCl in the solution used for interference testing of the MN glucose electrode. The addition of a certain concentration of a chemical at a specific time point is indicated by an arrow. (G–N) The amperometric response of the MN

(legend continued on next page)

(Figure 2O-1). The MN Na^+ electrodes were modified with a Na^+-ion-selective membrane that was evenly distributed after drying (Figure 2O-2). The MN reference electrode was coated with Ag/AgCl, where Ag/AgCl particles were uniformly dispersed on the electrode (Figures 2O and 3). The MN counter electrode possessed a Pt layer uniformly deposited on the MN surface (Figure 2O–4). The MN cholesterol electrode was modified with cholesterol oxidase (Figure 2O–5), and the MN uric acid electrode was coated with uric acid oxidase (Figure 2O–6). Similarly, K^+ ion-selective membrane-coated MNs served as the K^+ electrode (Figure 2O–7), and Ca^{2+} ion-selective membrane-coated Ca^{2+} was utilized as the Ca^{2+} electrode (Figure 2O–8). All the enzyme electrodes were cross-linked using a mixture of BSA and glutaraldehyde. Additionally, a Nafion membrane was employed as an outer membrane for the enzyme-based electrodes to prevent other interferences.

Electrochemical performance characterization of the MN electrodes

We conducted *in vitro* performance evaluations of the MN glucose electrode, MN uric acid electrode, MN lactate electrode, MN cholesterol electrode, MN ROS electrode, and MN ion electrode. An impermeable sealing membrane covered the top of the test vessel to simulate a stratum corneum layer. The MN electrode penetrated the membrane layer, and the tips were immersed in the test solution to detect the concentration of the analyte. The detection performance of enzyme-based amperometric electrodes, including the MN glucose electrode, MN uric acid electrode, MN lactic acid electrode, and MN cholesterol electrode, was evaluated. Using glucose detection as an example, the MN glucose electrode was tested via a three-electrode electrochemical system. The MN glucose electrode catalyzed glucose decomposition by enzymes on the surface of the electrodes. The electrons in the redox reaction were cotransferred to the electrode via the nanomaterials or H_2O_2 to generate the current signal for detection (Figures 3A and S3). The glucose concentration in the test mixture varied between 0 and 30 mM. This concentration range mimicked the *in vivo* environment and fully covered the range of glucose concentrations in the blood of hyperglycemic patients. A bias potential of 0.5 V was applied to the MN working electrode, and a steady (after a 2-min stabilization period) current signal was recorded. To further characterize the sensing performance of the MN electrode in glucose solutions, the amperometric response of the as-fabricated GOx/Pt/PEDOT:PSS/CNT/Au-MN electrode was evaluated across a concentration gradient ranging from 0 to 30 mM (Figure 3B). The sensitivity of the GOx/Pt/Au-MN electrode was determined to be 30.02 nA/mM with a linear range of 0–10 mM, whereas the GOx/Pt/CNT/Au-MN electrode exhibited a sensitivity of 35.20 nA/mM with a linear range of 0–12 mM. Furthermore, the Au/CNT/PEDOT:PSS/Pt/GOx MN electrode showed a sensitivity of 43.52 nA/mM, with a linear range extending up to 0–30 mM (Figure 3C). To investigate the electrocatalytic activity of the electrodes in the electrochemical processes, CV tests were conducted in a 5 mM glucose/PBS solution. Compared with the Au/Pt/GOx MN and Au/CNT/Pt/GOx MN electrodes, the Au/CNT/PEDOT:PSS/Pt/GOx MN electrode exhibited a higher current density (Figure 3D), indicating its excellent activity. Furthermore, we evaluated the electrode's current response curve with increasing glucose concentration in a continuous solution environment. This process was consistent with the intermittent collection of current versus concentration, further demonstrating the electrode's stability and reproducibility (Figure 3E). To verify the detection selectivity of glucose, 0.2 mM uric acid, 0.2 mM cholesterol, 2 mM lactic acid, 0.2 mM uric acid, 0.2 mM vitamin C, 1 mM KCl, 1 mM NaCl, 2 mM glucose, 1 mM $CaCl_2$, 2 mM lactic acid, 0.2 mM cholesterol, and 0.2 mM uric acid were sequentially added to the test solution, and the currents generated by these interference signals were found to be negligible compared with the glucose-induced signals (Figure 3F).

For uric acid sensing, similar to glucose detection, the MN electrode uses a three-electrode electrochemical system to convert the uric acid concentration to a current signal via uric acid oxidase. Uric acid at concentrations ranging from 0 to 1.0 mM was gradually added to the test solution (Figure 3G). When a bias potential of 0.3 V was applied, the current signal gradually increased with increasing uric acid concentration. The detection sensitivity was 3.74 ± 0.12 μA/mM, with a linear range >1.0 mM (Figure 3H). Lactate at concentrations ranging from 0 to 25 mM was gradually added to the test solution. When a bias potential of −0.4 V was applied, the current signal gradually increased with increasing lactate concentration. The detection sensitivity was −1.37 ± 0.46 μA/mM, with a linear range >25 mM (Figures 3I and 3J). Cholesterol concentrations ranging from 0 to 10 mM were gradually introduced into the test solution. When a bias potential of 0.3 V was applied, the current signal of the sensor linearly increased with increasing cholesterol concentration. The detection sensitivity was determined to be 0.36 ± 0.005 μA/mM, with a linear range exceeding 10 mM (Figures 3K and 3L). For ROS sensing, the surface of the MN electrode was modified with Pt nanocomposites. These nanocomposites could catalyze H_2O_2 to generate a current signal that was detected by an electrochemical three-electrode system. Since the *in vivo* ROS concentration ranged from 0 to 100 mM, H_2O_2 in the concentration range of 0–20 mM was used as a representative ROS for the experiments. When a −0.1-V bias voltage was applied, the amplitude of the recorded current signals increased linearly with increasing H_2O_2 concentration. The detection sensitivity was −5.66 ± 0.24 μA/mM, with an upper detection limit >20 mM (Figures 3M and 3N).

For ion sensing, the target ions (H^+, Na^+, K^+, and Ca^{2+}) have concentration differences inside and outside the ion-selective membrane coating the electrode surface. This resulted in a potential difference reflecting the ambient ions (Figure 3O). Since the transmembrane potential varies with the activity of the ion being measured, the concentration of the ion can be determined from the transmembrane potential of the ion-selective membrane. In particular, the ion-selective membrane possesses selective permeability to different ions. The coating of reference electrodes with PVB was beneficial for ensuring stable potentials across solutions of varying ionic strengths (Figure 3P). The incorporation of PEDOT:PSS as an ion-to-electron transducer within MN ion-selective electrodes could enhance the sensing performance.[39] The detection sensitivity for Na^+ was determined to be 63 ± 2.05 mV/(lg[Na^+]), with a high level of linearity (R^2 = 0.998). Three samples were concurrently tested, and excellent reproducibility was attained (Figure 3R). Similarly, in the case of K^+ sensing (Figure 3S), the concentration of K^+ increased incrementally from 2 to 32 mM, resulting in linear variation in the measured potential signals relative to the K^+ concentration. The detection sensitivity was calculated to be 48.06 ± 0.69 mV/(lg[K^+]), with a high level of linearity (R^2 = 0.996) and good reproducibility (Figure 3T). In the context of Ca^{2+} sensing (Figure 3U), the potential signal registered by the MN electrode displayed a linear correlation with the Ca^{2+} concentration across the range of 10–100 mM. The detection sensitivity was calculated as 19.53 ± 0.37 mV/(lg[Ca^{2+}]), with a linear goodness of fit represented by R^2 = 0.9995 and satisfactory reproducibility (Figure 3V). For pH sensing (Figure 3W), the pH in the solution gradually increased from 5 to 8, and the potential signal measured by the MN electrode increased linearly with the detection sensitivity, which was −54.35 ± 1.4 mV/(−lg[H^+]). The linear fit was R^2 = 0.998 for three electrodes tested in parallel, and good reproducibility was attained (Figure 3X). Furthermore, the electrochemical response of Na^+, K^+, and Ca^{2+} ion sensors to target and interfering substances (including NaCl, KCl, $CaCl_2$, $MgCl_2$, and NH_4Cl) was continuously monitored. The three electrodes produced only weak signals from the interfering ions and had little effect on the response signals in experiments with continuous immunity to interfering substances. Further quantification of the effect of each interfering agent produced no more than 20% of the interfering signal for each interferent (Figure S12). These results indicated that the MN ion electrodes possessed good selective sensing ability.

Next, we investigated the application of MN electrode arrays for detecting the spatial distribution of glucose concentrations in tissue. We used kiwifruit tissue as a model since the central part of kiwifruit possesses different sugar levels than the outer part of the pulp (Figure S13). The MN working electrodes in the array were functionalized as glucose electrodes to map 16 different positions on the cross-sectional surface of kiwifruit (marked with red circles). The detected current signals were then used to calculate the glucose concentration according to the *in vitro* signal-concentration curve, and the results revealed that the glucose concentrations ranged from 0.07 to 0.6 mM. The results were

electrodes for the detection of uric acid, lactate, cholesterol, and H_2O_2. The signal responses of these MN electrodes at different solution concentrations are presented (N = 3 per group). (O) Schematic representation of the MN electrodes for Na^+, K^+, Ca^{2+}, and H^+ ion sensing. The schematic shows the composition of each layer and its function. (P) Performance of the polyvinyl butyral (PVB)-protected MN Ag/AgCl electrode compared with that of the MN Ag/AgCl electrode in different concentrations of NaCl solution. (Q–X) Open-circuit potential response of the MN electrodes for Na^+, K^+, Ca^{2+}, and pH sensing, which correlates the logarithmic ion concentration with voltage (n = 3 for each group).

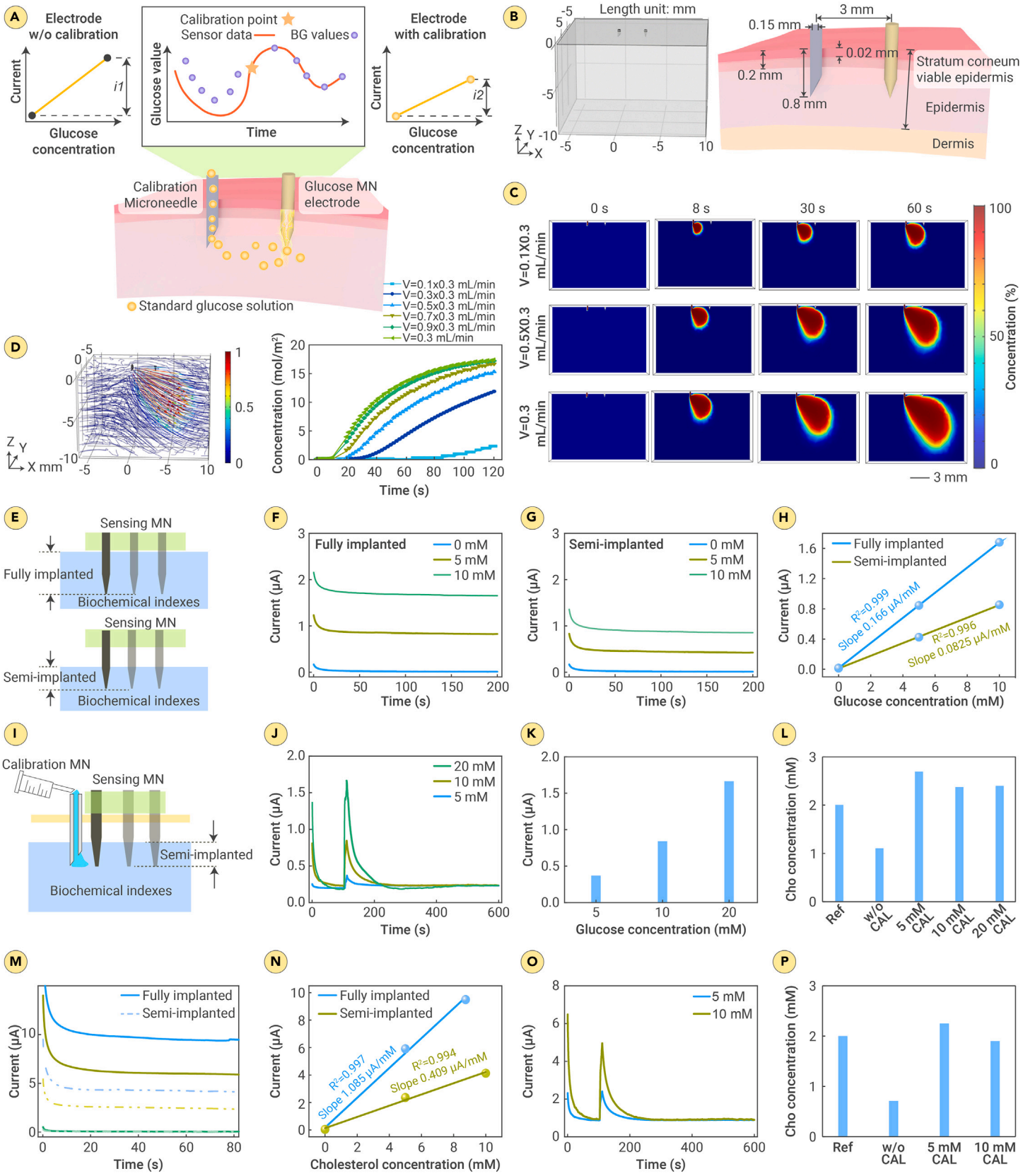

Figure 4. ***In vitro*** **self-calibration technique** (A) Working schematic of the hollow MN-mediated self-calibration technique. (B) COMSOL simulation modeling for calculating the mechanism of the MN-mediated self-calibration technique. An MN-sensing electrode and a hollow MN for delivery were used to penetrate a skin-tissue model. (C) Two-dimensional plots showing the COMSOL simulation results of the molecule diffusion profiles mediated by hollow-MN delivery. The concentration distributions at different times (0, 8, 30, and 60 s) and different flow rates (0.1 × 0.3, 0.5 × 0.3, and 0.3 mL/min) are presented. (D) Streamline plot representing the MN delivery concentration in the COMSOL simulation model. The results show the concentration distribution of glucose introduced subcutaneously through the hollow MNs at different times (0, 8, 30, and 60 s) and at different flow rates (0.1 × 0.3, 0.3 × 0.3, 0.5 × 0.3, 0.7 × 0.3, 0.9 × 0.3, and 0.3 mL/min). (E) Schematic diagram of MN-sensing electrodes extending 1.2 mm (indicated as full implantation of the MN) and 0.6 mm (indicating semi-implantation of the MN) into the solution for the detection of different concentrations of glucose and cholesterol. (F and G) I-t sensing curves of fully or semi-implanted MN glucose-sensing electrodes in response to the delivery of glucose/PBS solutions (0, 5, and 10 mM) as the calibration medium. (H) Current signal-versus-glucose-concentration curves for the MN glucose

(legend continued on next page)

normalized to determine the concentration distribution on the kiwifruit surface. The glucose concentration of the outer pulp part was significantly lower than that of the central part, and the boundary of the concentration difference was consistent with the boundary between the outer pulp part and the central area. Thus, these results validated the multipoint spatial collection and detection function of the MN electrode array.

Enzyme-based electrochemical electrodes were implanted subcutaneously for long-term monitoring of molecular species in tissue fluid. The activity of the enzyme modified on the electrode gradually decreased over time. Moreover, factors such as deviation of the transdermal MN electrode positions and interference from tissue fibrosis and inflammatory reactions in the complex biological environment could lead to changes in the sensing performance of the electrode and a decrease in detection sensitivity. Commercial implantable glucose electrodes typically require patients to perform fingerstick blood sampling daily for signal calibration of CGM to maintain accurate operation of the sensing electrode over time (Figure S14). To overcome the drawbacks of fingerstick blood sampling for calibration, we propose a hollow MN self-calibration technique that can calibrate the glucose detection signal of transdermal MN electrodes without blood sampling. This method uses hollow MNs to deliver a known concentration of glucose solution into the tissue fluid, and the neighboring MN electrochemical electrode quickly measures the glucose concentration in the local tissue fluid at the current moment. Thus, an accurate relationship between the electrochemical signal and the known glucose concentration could be obtained. The current signal-glucose concentration standard curve obtained by this method could be further used to calibrate the electrochemical signals recorded at other times, thereby correcting the measured glucose concentrations at other times (Figure 4A).

We used the chemical substance transfer module of COMSOL Multiphysics to simulate the process of hollow-MN delivery of labeled glucose solution. We constructed a simplified 3D model of skin tissue (with open boundaries), with different skin layer thicknesses of 0.02 mm (stratum corneum), 0.2 mm (active layer), and 2 mm (dermis). A solid MN electrode and a hollow-MN delivery electrode were inserted into the skin. The inner diameter of the hollow MNs was 0.15 mm, the distance between adjacent MNs was 3 mm, and the transdermal depth of the MNs was 0.8 mm (Figure 4B). The initial concentration of glucose in the tissue fluid was set to C0 (10 mol/m^3), and the concentration of glucose solution in the hollow MN channel was set to C1 (10 mM). Under the action of a peristaltic pump, the glucose solution flowed into the tissue fluid through the hollow MNs at a constant flow rate V0 and continuously diffused into the subcutaneous tissue (Figure 4C). Figure 4D shows the glucose concentration in the region near the MN electrode at different times (0–120 s) and different flow rates (0.1 × V0 to V0). As the flow rate of the glucose solution in the hollow MNs increased from 0.1 V0 to V0 (volume flow rate V0 = 0.3 mL/min, equivalent to a flow rate of 0.283 m/s), the glucose concentration in the tissue environment significantly increased, and the glucose concentration in the tissue near the MN electrode also increased (Figure S15). Next, we conducted simulation experiments on glucose solutions *in vitro* to verify the concept of this hollow MN self-calibration technique. As shown in Figure 4E, a solid-MN glucose electrode and a hollow-MN delivery electrode were inserted into the solution. To simulate the signal deviation caused by the insertion depth offset of the MN electrode, the length of the MN glucose electrode that was assumed to be completely inserted into the solution was 1.2 mm, and the length that was partially inserted into the solution was assumed to be 0.6 mm. For these two insertion depths, the MN electrode detected a series of glucose concentrations (0–10 mM). For the fully inserted condition, the sensitivity of MN electrode detection was 0.167 μA/mM, and the corresponding signal-concentration curve was Y = 0.167X + 0.0149, where X represents the glucose concentration and Y represents the current signal detected by the electrode. For the partially inserted state, the sensitivity of the MN electrode was 0.082 μA/mM, and the corresponding signal–concentration curve was Y = 0.08246X + 0.02679. These results indicated that the difference in the insertion depth of the MN electrode resulted in different signals recorded by the electrode and produced different signal-concentration standard curves for the same glucose solution (Figures 4F–4H). Next, the MN glucose electrode was inserted into a 2 mM glucose/PBS solution in a semi-inserted state (insertion depth of 0.6 mm) for continuous monitoring and then calibrated with labeled calibration solution through the hollow MN. Initially, within the first 100 s, the MN glucose electrode recorded the signal of a 2 mM glucose/PBS solution. In the first 100 s, the current signal gradually stabilized at 0.19871 μA. According to the standard curve of the fully inserted MNs, the concentration of glucose solution obtained was 1.1 mM. Thus, a large error was attained compared with the actual 2 mM glucose solution. After 100 s, a 5 mM glucose solution (for 10 s) was introduced through the hollow MNs, and the signal changes in the MN glucose electrode were separately recorded. The current signal of the MN electrode immediately increased, peaked (Imax), gradually decreased, and stabilized after 200 s. This occurred because the volume of the solution delivered by the hollow MNs was only 50 μL, and the additional glucose delivered by the solution quickly diffused into the solution. After a 5 mM standard glucose solution was introduced through the hollow MNs, the obtained Imax was 0.3688 μA. This value differed from the current signal of 0.8444 μA measured by the MN electrode exposed to a 5 mM glucose solution (Figures 4I and 4J). By correcting this difference and calculating the current signal of the MN electrode before the standard solution was added, the original glucose concentration in the solution was determined to be 2.69 mM. The original glucose concentration measured by the MN electrode before calibration was 1.1 mM. After calibration with a 5 mM standard glucose solution delivered by the hollow MNs, the glucose concentration measured by the MN electrode was closer to the actual value of 2 mM. Similarly, if a 10 or 20 mM glucose solution was introduced through the hollow MNs for calibration, the obtained Imax values were 0.8406 and 1.6653 μA, respectively. After calibration, the glucose concentrations measured by the MN electrode were 2.36 and 2.39 mM. These values were closer to the actual concentration of 2 mM in the original glucose solution (Figure 4K). Notably, the calibration delivery solutions were analyzed within 2 min. Therefore, the effect of the metabolism of the molecules is negligible. On the other hand, the diffusion of molecules needs to be considered. In the experiments, the calibration signals were collected at t = 100 s after delivery as a standard procedure. Since the diffusion time in every set of experiments was identical, the variation in chemical concentrations could be avoided.

Similarly, we conducted *in vitro* experiments utilizing cholesterol solutions to verify the feasibility of the hollow MN self-calibration technique for cholesterol delivery. A solid-MN cholesterol electrode and a hollow-MN delivery electrode were immersed into the solutions in both the semi-insertion (insertion length of 0.6 mm) and full-insertion (insertion length of 1.2 mm) states. Across these insertion depths, the MN electrodes detected cholesterol concentrations ranging from 0 to 8.75 mM (Figures 4L and 4M). Notably, under fully inserted conditions, the sensitivity of MN electrode detection was 1.085 μA/mM, whereas, for the semi-inserted state, it was 0.409 μA/mM (Figure 4N). Consequently, the discrepancy in the MN electrode insertion depth manifests as a discernible impact on the signal intensity for identical cholesterol solutions. The MN cholesterol electrode, configured in the semi-insertion state, was subsequently subjected to continuous monitoring within a 2 mM cholesterol/PBS solution. This was followed by calibration procedures employing standard cholesterol calibration solutions delivered through the hollow MNs. Initial recordings within the first 100 s yielded a signal corresponding to 2 mM cholesterol, quantified at 0.9497 μA. However, theoretical calculations based on standard curves for fully inserted MNs estimated the cholesterol solution concentration at 0.71 mM. These results were notably different from the actual 2 mM cholesterol concentration. After the initial 100-s period, sequential introductions of 5 and 10 mM cholesterol solutions using the hollow MNs were carried out, each lasting for 10 s (Figure 4O). Subsequent monitoring of the signal changes by the MN cholesterol electrode facilitated the calibration procedures. Following calibration with the 5 and 10 mM

electrodes in fully implanted and semi-implanted states. (I) Schematic diagram showing MN-mediated calibration for *in vitro* monitoring experiments. (J) During continuous sensing in a 2 mM glucose/PBS solution, the i-t curves of the MN glucose-sensing electrode were recorded. At t = 100 s, the glucose calibration solution (5, 10, or 20 mM) was introduced, and the response of the MN electrode was monitored. (K) Maximum current signals detected by the MN electrode for three glucose calibration solutions (5, 10, and 20 mM). (L) Detected glucose concentration in solution according to the MN electrode signals before and after delivery-mediated calibration. (M) i-t sensing curve of the fully or semi-implanted MN glucose-sensing electrode in response to the delivery of cholesterol/PBS solutions (0, 5, and 8.75 mM) as the calibration medium. (N) Current signal-versus-cholesterol-concentration curves for the MN cholesterol electrodes in fully implanted and semi-implanted states. (O) During continuous sensing in a 2 mM cholesterol/PBS solution, the i-t curves of the MN cholesterol-sensing electrode were recorded. At t = 100 s, cholesterol calibration solution (5 or 10 mM) was introduced, and the response of the MN electrode was monitored. (P) Detected cholesterol concentration in solution according to the MN electrode signals before and after delivery-mediated calibration.

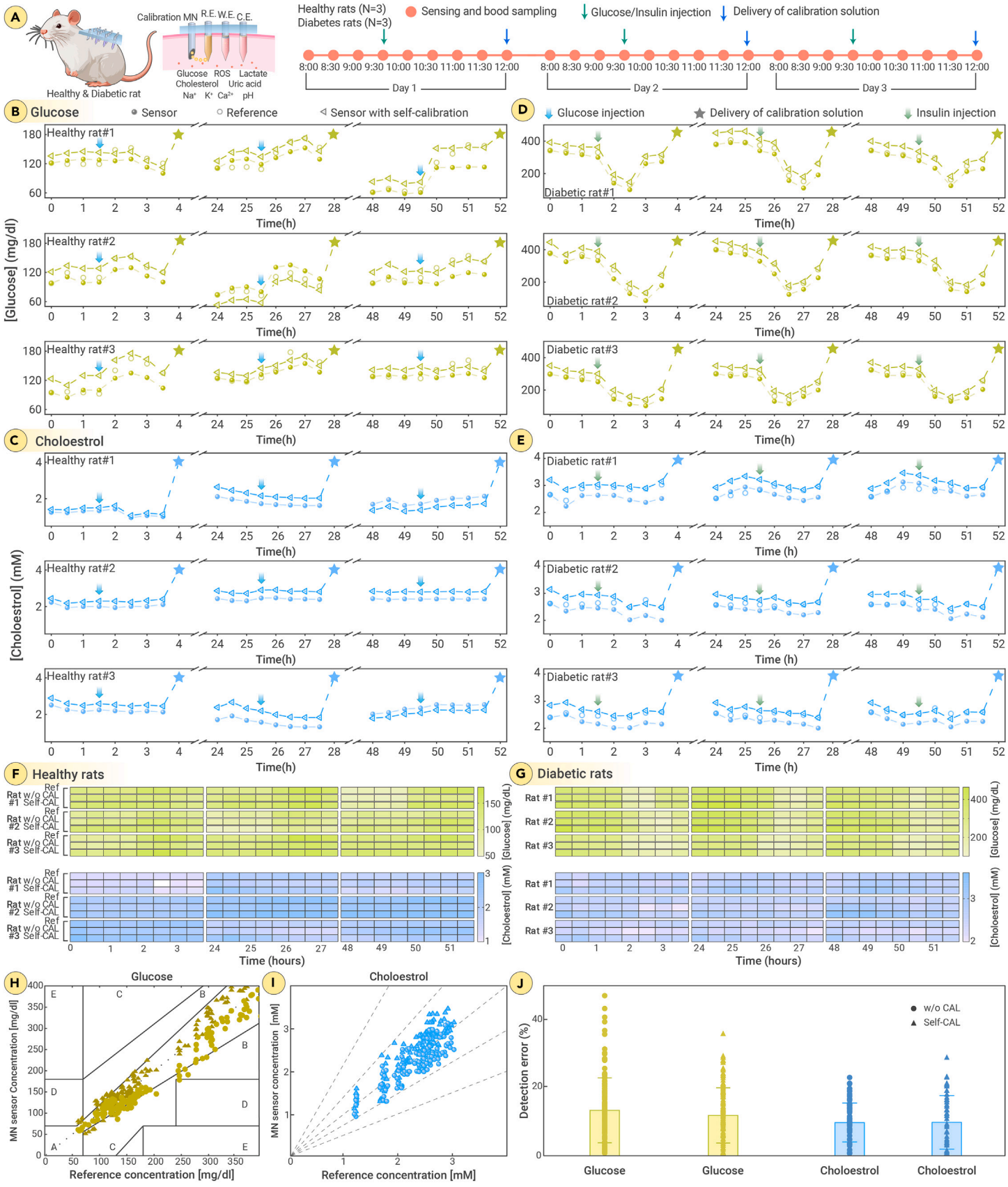

Figure 5. Characterization of the *in vivo* sensing performance of SC-MMNEA (A) Schematic of the application of the MN electrodes in rats to monitor the bioanalyte concentrations in the subcutaneous space. MN sensing was performed for 4 h per day for three consecutive days. The model group included healthy control rats and diabetic rats (n = 3 for each group). The MN-detected bioanalyte concentrations were compared with those of standard reference methods to assess accuracy. Blood samples were drawn from the rat tail vein to measure the accurate concentrations of each analyte via a commercial biochemical analyzer. The MN-detected glucose and cholesterol concentrations were calibrated via hollow-MN-mediated delivery. (B–E) MN electrode-detected glucose and cholesterol signals in healthy and diabetic rats. The arrows indicate glucose or insulin injections, the solid dots indicate the MN sensing results, the hollow dots indicate reference concentrations, and the asterisks indicate hollow-MN-delivery-mediated calibration data points. (F) and (G) Data in

(legend continued on next page)

standard cholesterol solutions delivered through the hollow MNs, the original cholesterol concentrations within the solution were determined to be 2.25 and 1.90 mM, respectively (Figure 4P). These values closely approximated the actual concentration of 2 mM within the original cholesterol solution. Figure 4Q shows the module block diagram of the SC-MMNEA detection circuit. The circuit contains several components, including a microcontroller unit (8), a power management module (1–3), a serial communication module (1), and an analog signal conditioning module (4–7). The whole hardware circuit attained the acquisition, processing, and transmission of five current signals for glucose, cholesterol, uric acid, lactic acid, and active oxygen detection and four potential signals for Na^+-, K^+-, and Ca^{2+}–ion and pH detection. The power management module provided appropriate operating voltages for the different components of the circuit. After amplification, filtering, and offsetting by the analog signal conditioning module, the signals collected by the multiparameter biosensor generated potential signals associated with metabolite concentrations and were input to the microcontroller unit. Under the control of the microcontroller unit, the potential signal was converted to a digital signal by an analog-to-digital converter, and further data processing and temporary storage were performed. Finally, the stored digital signals are transferred to the software host computer via a USB cable through the serial communication module. The final data processing, display, and storage steps were performed (Figures S16–S23).

In vivo sensing performance of SC-MMNEA

Following the preliminary *in vitro* investigations, we proceeded with *in vivo* experimentation to validate the capability of MMNEA for continuous monitoring of diverse chemical indices within the ISF milieu. Sprague-Dawley rats were used as the experimental model. After depilation of the dorsum and anesthesia, the MN array was meticulously inserted through the skin and affixed onto the dorsal region of the rats for monitoring purposes. Since the size of the rats was significantly smaller than that of the human body, the 4 × 4 MN electrode array was impractical and difficult to fix on the curved dorsal skin of the rats in the experiment. Alternatively, the 4 × 4 array of integrated MN sensors was modified into four separate sets of 2 × 2 arrays to facilitate flexible attachment of the MN device onto the dorsal skin of the rats (Figure 5A). These MN electrodes in the array were engineered to collectively detect nine types of chemical indices, namely glucose, cholesterol, uric acid, lactate, ROSs, Na^+, K^+, Ca^{2+}, and pH. MMNEA was utilized to monitor the bioanalytes in the ISF of the anesthetized rats at 30-min intervals, and data acquisition was conducted concomitantly at each MN electrode reading. Concurrently, blood samples were drawn from the rat tail vein, and the concentrations of the nine types of analytes therein were quantified via commercial biochemical analyzers to serve as reference data for comparative analysis with the MN array sensing results. Considering the limitations imposed by the anesthetized state, instead of 24-h continuous monitoring, the experimental sessions were confined to 4-h durations per day, spanning three consecutive days. At the end of each daily experiment, the rats were allowed to recover from the anesthesia state, and the MN array was withdrawn to allow the rats to return to the cage after each set of experiments. The MN array was reapplied to the rat for the sensing experiment the next day. During each experimental session, normoglycemic rats received intraperitoneal injections of glucose solution at the 1.5-h mark to prompt fluctuations in blood glucose levels. Conversely, diabetic rats induced with streptozotocin were administered subcutaneous injections of insulin solution at the same time points to assess alterations in chemical indices under insulin treatment. Moreover, to assess the applicability of the MN self-calibration technique *in vivo*, injections of a mixed solution comprising 10 mM glucose and 4 mM cholesterol were administered to normoglycemic rats, whereas injections of a mixed solution containing 25 mM glucose and 4 mM cholesterol, which served as calibration solutions, were administered to diabetic rats at the end of the 4-h recording of each day's experimentation. The current signals of the MN sensors were recorded postinjection of the calibration solutions. The blood glucose concentrations of three normoglycemic rats increased within 30 min after glucose injection (denoted by the red arrows in Figure 5B), followed by a decrease to basal levels within the subsequent 1.5 h (depicted by the gray shaded bands). Similar recordings were collected for changes in cholesterol concentrations in normoglycemic rats (Figure 5C). In diabetic rats, insulin administration (indicated by the green arrows in Figure 5D) induced reductions in blood glucose levels to euglycemic levels within 0.5–1 h post administration (represented by the light red bands, with blood glucose concentrations ranging from 100 to 200 mg/dL), and the blood glucose levels were sustained at euglycemic levels for approximately 2–3 h before reverting to hyperglycemic states. The corresponding data of the changes in cholesterol levels in diabetic rats were recorded (Figure 5D), and the changes in glucose and cholesterol concentrations after self-calibration were further determined (depicted by triangular curves in Figures 5B–5E). All the results were additionally analyzed via heatmaps (Figures 5F and 5G), and darker blocks indicate the detection of elevated glucose levels. The cholesterol concentrations appeared to be less affected by the glucose injections, potentially because the transient increase in glucose levels was insufficient to impact renal and hepatic functions in normoglycemic rats. Thus, significant disturbances in cholesterol levels within the body did not occur. Data analysis was initially performed on the *in situ* monitoring of glucose and cholesterol concentrations from all the rats, and the results were compared with values obtained through single-drop blood calibration and those from MN self-calibration. By using error grid analysis, all MN-recorded glucose (Figure 5H) and cholesterol (Figure 5I) data resided within the A zone (less than 15%), indicating high detection accuracy. Furthermore, the errors in the glucose signals measured by MN self-calibration were less than ∼12.84%, with an average error of 12.84% ± 9.68% for single-drop blood calibration and 11.33% ± 8.24% post self-calibration, satisfying the clinical requirements for blood glucose testing error (<15%). After single-drop blood calibration and self-calibration, the average errors for cholesterol were 9.62% ± 6.50% and 9.43% ± 8.37%, respectively (Figure 5J). These findings highlight the ability of MN sensors to detect glucose and cholesterol concentrations accurately in ISF, while the employment of MN self-calibration techniques enhances the accuracy of long-term monitoring of MN electrodes.

We subsequently examined other MN-recorded data of bioanalytes, including lactate, uric acid, ROS, Na^+, K^+, Ca^{2+}, and pH data, from both healthy and diabetic rats. The data were analyzed via heatmaps and scatterplots, and the results measured by the MN electrode were compared with the reference values (Figures 6A and S24–S29). Error grid analysis revealed that lactate, uric acid, and pH measurements acquired via the MMNEA predominantly resided within the A zone (below 20% deviation), and the ROSs only had a few data points within the B zone (20%–50%). This outcome highlighted the exceptional accuracy of the electrodes in sensing these biochemical indices (Figure 6B). After one-point blood calibration, the mean errors in the lactate, uric acid, and ROS signals measured by the MMNEA were 6.20% ± 5.05%, 8.42% ± 6.62%, and 11.28% ± 10.52%, respectively. Following two-point calibration for Na^+, K^+, Ca^{2+}, and pH, the mean errors in the signals were 17.32% ± 18.63%, 17.37% ± 15.33%, 19.60% ± 16.40%, and 3.34% ± 3.13%, respectively. Notably, deviations exceeding 50% existed among the concentrations of Na^+, K^+, and Ca^{2+} obtained through one-point calibration and those measured by reference methods. This could be attributed to some differences in ion concentrations between ISF and blood environments. These findings collectively indicate that MN electrodes have the capacity to detect the concentrations of lactate, uric acid, ROSs, Na^+, K^+ and Ca^{2+} and the pH within the tissue fluid *in situ*. To explore the response of healthy rats to glucose fluctuations and the subsequent metabolic changes that occur in diabetic rats following insulin therapy, we analyzed the concentrations of nine bioanalytes before and after injection in both groups of rats (Figure S30). Following glucose injection in healthy rats, blood glucose levels increased from 102.69 to 139.15 mg/dL, with minor changes in the concentrations of the remaining indicators. In diabetic rats, after insulin injection, blood glucose levels decreased from hyperglycemic (325.37 mg/dL) to normal (173.13 mg/dL). The values measured by the SC-MMNEA were compared with the reference values, and a radar chart was created (Figure S31). In healthy rats, the concentrations of glucose, lactate, uric acid, and other metabolic indices remained relatively low during the initial 2-h window preceding glucose induction. A discernible increase

(B)–(E) are presented as heatmaps to show the dynamic fluctuations in glucose (upper panel) and cholesterol (lower panel) concentrations in healthy and diabetic rats. The results included reference concentrations and sensor-detected concentrations without or with self-calibration. (H) Clarke's error grid analysis showing the accuracy of glucose sensing by the MN electrodes compared with actual blood glucose levels measured by a standard glucose meter. (I) Error grid analysis showing the accuracy of cholesterol sensing by MN electrodes compared with bioanalyzer measurements. (J) Statistical analysis showing the detection error of the glucose concentration and cholesterol concentration detected by the MN electrode compared with the reference method. The data are expressed as the means ± SEMs.

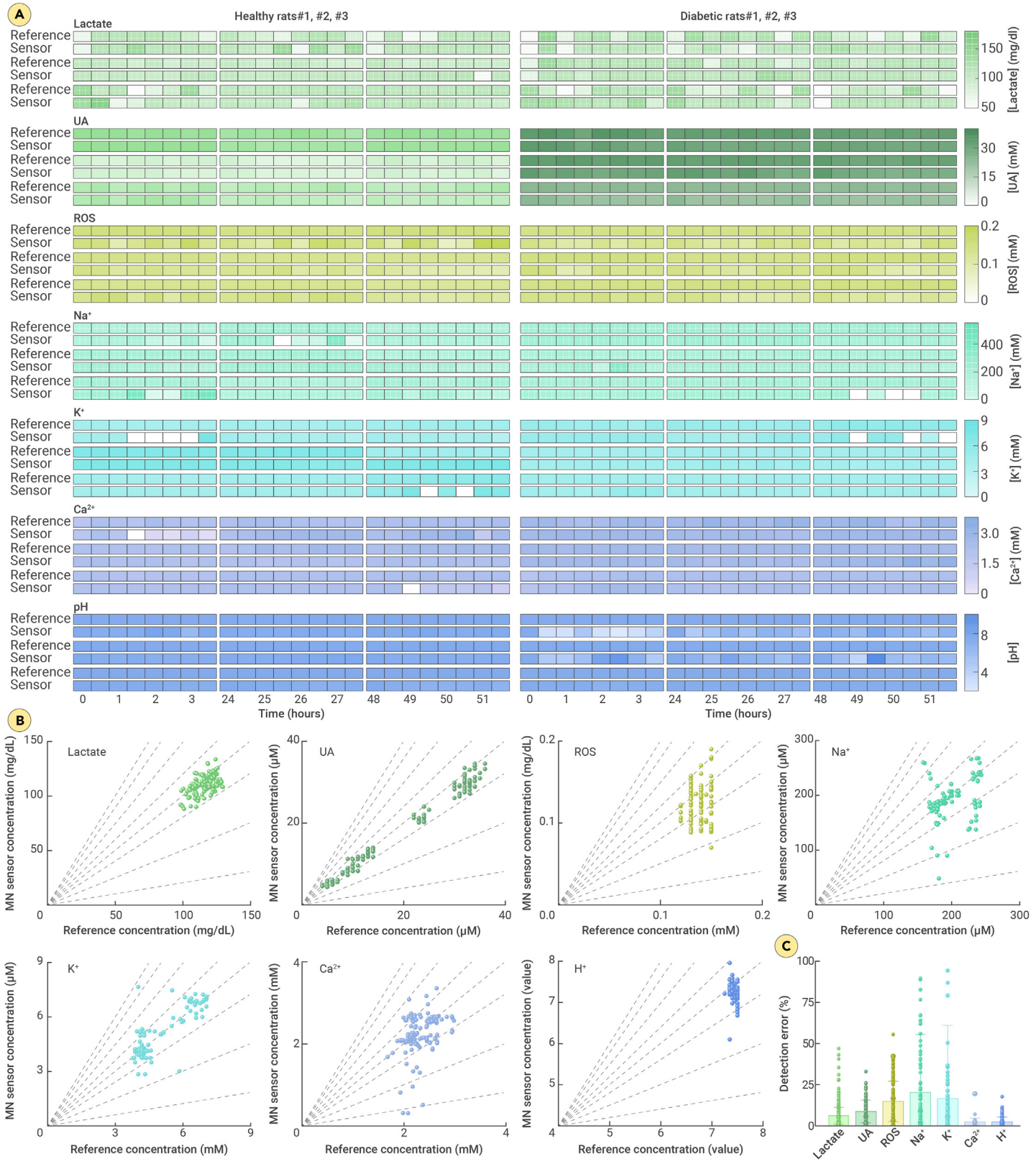

Figure 6. Characterization of the *in vivo* sensing performance of SC-MMNEA for other bioanalytes (A) MN electrode detection of lactate, uric acid, reactive oxygen species (ROSs), Na^+, K^+, Ca^{2+}, and pH signals in healthy and diabetic rats. The results were compared with those of reference methods. The results are presented as heatmaps to show the dynamic fluctuations in analyte concentrations in healthy and diabetic rats. The results included reference concentrations and sensor-detected concentrations. (B) Clarke's error grid analysis showing the accuracy of the MN-recorded data of bioanalytes compared with the reference measurements. Regions A + B, C, and D indicate errors <20%, 20%–40%, and >40%, respectively. (C) Statistical analysis showing the detection error of the MN-recorded data from lactate, uric acid, ROSs, Na^+, K^+, and Ca^{2+} and the pH compared with the reference measurements. The data are expressed as the means ± SEMs.

in glucose concentration subsequently occurred after glucose induction. These results indicated a transient increase in blood glucose levels prompted by exogenous glucose infusion. Conversely, the concentrations of other metabolic indices, such as lactate, uric acid, cholesterol, ROSs, Na^+, K^+, Ca^{2+}, and pH, remained largely unaltered. These observations highlight the ability of healthy rats to maintain normal metabolic states, barring transient glucose elevation

induced by direct glucose infusion, with minimal perturbations observed in other bioanalytes. In the initial 2 h before insulin injection, the average concentrations of glucose in diabetic rats were greater than those in healthy rats. After insulin injection, the glucose concentration in diabetic rats decreased, indicating a reduction in blood glucose levels to a controllable range. However, in comparison with those in healthy rats, the concentrations of other bioanalytes, such as uric acid and cholesterol, continued to be elevated in diabetic rats, whereas no significant changes were observed in the ROSs, Na^+, K^+, Ca^{2+}, or pH data. This phenomenon was likely attributed to the protracted metabolic dysregulation induced by diabetes, whereby transient intervention failed to rectify the persistently elevated levels of these two bioanalytes in diabetic rats.

To expand the use of SC-MMNEA for further product applications, some important treatment procedures involving electrodes and devices are needed. The device usually requires UV sterilization or irradiation sterilization. The manufacturing and distribution challenges are related mainly to the reproducibility of the device during the standard manufacturing process. The homogeneity of the coating preparation and the consistency of the sensor batches need to be further optimized for industrial production. Specialized storage of the device in a N_2 atmosphere at low temperature is needed. This could prevent degradation of the device. The device is for one-time use and is not supposed to be used repeatedly. The patient can insert the MN device by hand to complete the subcutaneous puncture without assistance from the nurse. The developed metal MN electrodes can be easily pierced into the subcutaneous area, which is an advantage over conventional polymer MNs. The resistance of the MN electrode after insertion under the skin can be detected to determine whether the MN electrode is conducting. MNs that do not penetrate into the skin usually have higher resistance at the skin surface, and the resistance could be used to determine the insertion of MNs into the skin. After piercing subcutaneously, a warm-up start-up time of 0.5–2 h is usually needed. This amount of time is also commonly required for current commercial CGM. This time frame allows sufficient diffusion of ISF into the functional layers of MNs. Since SC-MMNEA provides long-term continuous monitoring, it is fundamentally different from the single test of glucose test strips, which uses only one data point. When the device is used, it can be disposed of as regular medical waste, such as the disposal of bandages, hemostatic tapes, or commercial CGM. To increase the stability, the electrodes are usually protected by a diffusion-limiting outer membrane to prevent leakage of the electrode material, and CGM also uses some carbon e-ink as an electrode material, similar to the safety of CNTs. The outer membrane was Nafion, which is a diffusion-restricted membrane that allows the diffusion of glucose while preventing negatively charged macromolecules such as proteins. In addition, other macromolecules, such as polyurethane (PU) and zwitterionic polymers, can be used. This outer membrane technology has been successfully applied in commercial CGM and can effectively stabilize electrodes. Thus, the safety and biocompatibility of electrode materials can be ensured.

CONCLUSION

In summary, SC-MMNEA was developed as a versatile tool for continuous, real-time monitoring of multiple analytes in the subcutaneous space. Specifically, SC-MMNEA provides continuous monitoring of critical analytes in the ISF, including glucose, cholesterol, uric acid, lactate, ROSs, Na^+, K^+, and Ca^{2+}, and pH. The detection of these analytes *in situ* is beneficial for understanding the health and physiological state of patients with diabetic complications. The MN array was fabricated via a hybrid fabrication strategy through dimensional reduction fabrication and assembly of a discrete MN electrode. This strategy simplified the complexity of fabricating a 3D MN electrode array with single-needle detection resolution. Through this fabrication strategy, the MN electrodes could be flexibly combined to form the desired sensor array, and each MN electrode in the array could be readily withdrawn and replaced with a new electrode according to need. Moreover, the SC-MMNEA integrated a hollow-MN delivery module that could provide self-calibration to correct the electrical signals of analytes *in vivo*. This module could solve the inherent problems of decreased accuracy of subcutaneous electrodes during long-term tissue implantation or enzyme degradation. The methodology of MN-delivery-mediated self-calibration was validated by both COMSOL simulation and *in vitro* experiments. Moreover, the functionalities of SC-MMNEA were demonstrated *in vivo* in a rat model, and the results indicated that SC-MMNEA could provide continuous recordings of multiplexed analyte concentrations *in situ* and that the recording accuracy could be enhanced via MN-delivery-mediated self-calibration. Overall, SC-MMNEA is a promising tool that could enable real-time monitoring of multiplexed analytes in the subcutaneous tissue space in a safe and minimally invasive way, and the detection targets could be readily extended to other types of molecules in addition to the representative analytes demonstrated in this work.

REFERENCES

1. Xourafa, G., Korbmacher, M., and Roden, M. (2024). Inter-organ crosstalk during development and progression of type 2 diabetes mellitus. Nat. Rev. Endocrinol. ***20***: 27–49. https://doi.org/10.1038/s41574-023-00898-1.
2. Sims, E.K., Carr, A.L.J., Oram, R.A., et al. (2021). 100 years of insulin: celebrating the past, present and future of diabetes therapy. Nat. Med. ***27***: 1154–1164. https://doi.org/10.1038/s41591-021-01418-2.
3. Nusinovich, Y. (2021). A century of progress. Science ***373***: 504. https://doi.org/10.1126/science.abk0256.
4. Xiang, L., Wang, L., Xia, Y., et al. (2024). Exercise alleviates diabetic kidney disease through PPARδ-CPT1α pathway-dependent fatty acid β-oxidation. Innov. Life ***2***: 100065. https://doi.org/10.59717/j.xinn-life.2024.100065.
5. Gao, Y.-Z., Wang, Y., Ji, M., et al. (2023). A whole-cell hydrogen peroxide biosensor and its application in visual food analysis. Innov. Life ***1***: 100011. https://doi.org/10.59717/j.xinn-life.2023.100011.
6. Perkins, B.A., Sherr, J.L., and Mathieu, C. (2021). Type 1 diabetes glycemic management: Insulin therapy, glucose monitoring, and automation. Science ***373***: 522–527. https://doi.org/10.1126/science.abg4502.
7. Darrow, J.J., Van de Wiele, V., Beran, D., et al. (2023). An Empirical Review of Key Glucose Monitoring Devices: Product Iterations and Patent Protection. J. Diabetes Sci. Technol. ***19***: 19322968231178016. https://doi.org/10.1177/19322968231178016.
8. Garg, S.K. (2023). Past, present, and future of continuous glucose monitors. Diabetes Technol. Therapeut. ***25***: S1–S4. https://doi.org/10.1089/dia.2023.0041.
9. Li, X., Huang, X., Mo, J., et al. (2021). A Fully Integrated Closed-Loop System Based on Mesoporous Microneedles-Iontophoresis for Diabetes Treatment. Adv. Sci. ***8***: 2100827. https://doi.org/10.1002/advs.202100827.
10. Xie, X., Doloff, J.C., Yesilyurt, V., et al. (2018). Reduction of measurement noise in a continuous glucose monitor by coating the sensor with a zwitterionic polymer. Nat. Biomed. Eng. ***2***: 894–906. https://doi.org/10.1038/s41551-018-0273-3.
11. Sang, M., Cho, M., Lim, S., et al. (2023). Fluorescent-based biodegradable microneedle sensor array for tether-free continuous glucose monitoring with smartphone application. Sci. Adv. ***9***: eadh1765. https://doi.org/10.1126/sciadv.adh1765.
12. Yu, J., Wang, J., Zhang, Y., et al. (2020). Glucose-responsive insulin patch for the regulation of blood glucose in mice and minipigs. Nat. Biomed. Eng. ***4***: 499–506. https://doi.org/10.1038/s41551-019-0508-y.
13. Abramson, A., Caffarel-Salvador, E., Khang, M., et al. (2019). An ingestible self-orienting system for oral delivery of macromolecules. Science ***363***: 611–615. https://doi.org/10.1126/science.aau2277.
14. Teymourian, H., Tehrani, F., Mahato, K., et al. (2021). Lab under the Skin: Microneedle Based Wearable Devices. Adv. Healthcare Mater. ***10***: 2002255. https://doi.org/10.1002/adhm.202002255.
15. Tran, K.T.M., Gavitt, T.D., Farrell, N.J., et al. (2021). Transdermal microneedles for the programmable burst release of multiple vaccine payloads. Nat. Biomed. Eng. ***5***: 998–1007. https://doi.org/10.1038/s41551-020-00650-4.
16. Yu, J., Zhang, Y., Ye, Y., et al. (2015). Microneedle-array patches loaded with hypoxia-sensitive vesicles provide fast glucose-responsive insulin delivery. Proc. Natl. Acad. Sci. USA ***112***: 8260–8265. https://doi.org/10.1073/pnas.1505405112.
17. Zhi, D., Yang, T., Zhan, T., et al. (2021). Microneedles for gene and drug delivery in skin cancer therapy. J. Contr. Release ***335***: 158–177. https://doi.org/10.1016/j.jconrel.2021.05.009.
18. Babity, S., Roohnikan, M., and Brambilla, D. (2018). Advances in the Design of Transdermal Microneedles for Diagnostic and Monitoring Applications. Small ***14***: e1803186. https://doi.org/10.1002/smll.201803186.
19. Bollella, P., Sharma, S., Cass, A.E.G., et al. (2019). Microneedle-based biosensor for minimally-invasive lactate detection. Biosens. Bioelectron. ***123***: 152–159. https://doi.org/10.1016/j.bios.2018.08.010.
20. Dervisevic, M., Alba, M., Adams, T.E., et al. (2021). Electrochemical immunosensor for breast cancer biomarker detection using high-density silicon microneedle array. Biosens. Bioelectron. ***192***: 113496. https://doi.org/10.1016/j.bios.2021.113496.
21. Kim, J., Campbell, A.S., de Ávila, B.E.F., et al. (2019). Wearable biosensors for healthcare monitoring. Nat. Biotechnol. ***37***: 389–406. https://doi.org/10.1038/s41587-019-0045-y.
22. Dervisevic, M., Alba, M., Prieto-Simon, B., et al. (2020). Skin in the diagnostics game: Wearable biosensor nano- and microsystems for medical diagnostics. Nano Today ***30***: 100828. https://doi.org/10.1016/j.nantod.2019.100828.
23. Chen, Z., Lin, Y., Lee, W., et al. (2018). Additive Manufacturing of Honeybee-Inspired Microneedle for Easy Skin Insertion and Difficult Removal. ACS Appl. Mater. Interfaces ***10***: 29338–29346. https://doi.org/10.1021/acsami.8b09563.
24. Zheng, M., Sheng, T., Yu, J., et al. (2023). Microneedle biomedical devices. Nat. Rev. Bioeng. ***2***: 324–342. https://doi.org/10.1038/s44222-023-00141-6.
25. Ibrahim, N.E.-S. (2023). On-the-go blood glucose monitoring. Nat. Rev. Bioeng. ***1***: 465. https://doi.org/10.1038/s44222-023-00091-z.

26. Vora, L.K., Sabri, A.H., McKenna, P.E., et al. (2023). Microneedle-based biosensing. Nat. Rev. Bioeng. ***2***: 64–81. https://doi.org/10.1038/s44222-023-00108-7.
27. Palmer, B.F., and Clegg, D.J. (2015). Electrolyte and acid–base disturbances in patients with diabetes mellitus. N. Engl. J. Med. ***373***: 548–559. https://doi.org/10.1056/NEJMra1503102.
28. Pipeleers, L., Wissing, K.M., and Hilbrands, R. (2019). Acid-base and electrolyte disturbances in patients with diabetes mellitus. Acta Clin. Belg. ***74***: 28–33. https://doi.org/10.1080/17843286.2018.1546983.
29. Wu, M., Huang, X., Yan, D., et al. (2020). Interactions among endotoxin, uric acid, and lactate in relation to the risk of type 2 diabetes: A population-based study. J. Diabetes ***12***: 605–615. https://doi.org/10.1111/1753-0407.13039.
30. Katsiki, N., Dimitriadis, G.D., and Mikhailidis, D.P. (2021). Serum uric acid and diabetes: from pathophysiology to cardiovascular disease. Curr. Pharmaceut. Des. ***27***: 1941–1951. https://doi.org/10.2174/1381612827666210104124320.
31. Menè, P., and Punzo, G. (2008). Uric acid: bystander or culprit in hypertension and progressive renal disease? J. Hypertens. ***26***: 2085–2092. https://doi.org/10.1097/HJH.0b013e32830e4945.
32. Bhatti, J.S., Sehrawat, A., Mishra, J., et al. (2022). Oxidative stress in the pathophysiology of type 2 diabetes and related complications: Current therapeutics strategies and future perspectives. Free Radic. Biol. Med. ***184***: 114–134. https://doi.org/10.1016/j.freeradbiomed.2022.03.019.
33. Jalal, D.I., Rivard, C.J., Johnson, R.J., et al. (2010). Serum uric acid levels predict the development of albuminuria over 6 years in patients with type 1 diabetes: findings from the Coronary Artery Calcification in Type 1 Diabetes study. Nephrol. Dial. Transplant. ***25***: 1865–1869. https://doi.org/10.1093/ndt/gfp740.
34. Xia, Q., Zhang, S.-H., Yang, S.-M., et al. (2020). Serum uric acid is independently associated with diabetic nephropathy but not diabetic retinopathy in patients with type 2 diabetes mellitus. J. Chin. Med. Assoc. ***83***: 350–356. https://doi.org/10.1097/jcma.0000000000000285.
35. Bartáková, V., Kuricová, K., Pácal, L., et al. (2016). Hyperuricemia contributes to the faster progression of diabetic kidney disease in type 2 diabetes mellitus. J. Diabet. Complicat. ***30***: 1300–1307. https://doi.org/10.1016/j.jdiacomp.2016.06.002.
36. Bariya, M., Nyein, H.Y.Y., and Javey, A. (2018). Wearable sweat sensors. Nat. Electron. ***1***: 160–171. https://doi.org/10.1038/s41928-018-0043-y.
37. Davis, N., Heikenfeld, J., Milla, C., et al. (2024). The challenges and promise of sweat sensing. Nat. Biotechnol. ***42***: 860–871. https://doi.org/10.1038/s41587-023-02059-1.
38. Kim, J., Jeerapan, I., Sempionatto, J.R., et al. (2018). Wearable bioelectronics: Enzyme-based body-worn electronic devices. Acc. Chem. Res. ***51***: 2820–2828.
39. Waltz, E. (2019). Sweet sensation. Nat. Biotechnol. ***37***(4): 340–344. https://doi.org/10.1038/s41587-019-0086-2.
40. Yang, J., Zheng, S., Ma, D., et al. (2022). Masticatory system–inspired microneedle theranostic platform for intelligent and precise diabetic management. Sci. Adv. ***8***: eabo6900. https://doi.org/10.1126/sciadv.abo6900.
41. Gao, W., Emaminejad, S., Nyein, H.Y.Y., et al. (2016). Fully integrated wearable sensor arrays for multiplexed in situ perspiration analysis. Nature ***529***: 509–514. https://doi.org/10.1038/nature16521.
42. Ye, C., Wang, M., Min, J., et al. (2024). A wearable aptamer nanobiosensor for non-invasive female hormone monitoring. Nat. Nanotechnol. ***19***: 330–337. https://doi.org/10.1038/s41565-023-01513-0.
43. Tu, J., Min, J., Song, Y., et al. (2023). A wireless patch for the monitoring of C-reactive protein in sweat. Nat. Biomed. Eng. ***7***: 1293–1306. https://doi.org/10.1038/s41551-023-01059-5.
44. Teymourian, H., Barfidokht, A., and Wang, J. (2020). Electrochemical glucose sensors in diabetes management: an updated review (2010–2020). Chem. Soc. Rev. ***49***: 7671–7709. https://doi.org/10.1039/D0CS00304B.
45. Goud, K.Y., Moonla, C., Mishra, R.K., et al. (2019). Wearable electrochemical microneedle sensor for continuous monitoring of levodopa: toward Parkinson management. ACS Sens. ***4***: 2196–2204. https://doi.org/10.1021/acssensors.9b01127.
46. Tehrani, F., Teymourian, H., Wuerstle, B., et al. (2022). An integrated wearable microneedle array for the continuous monitoring of multiple biomarkers in interstitial fluid. Nat. Biomed. Eng. ***6***: 1214–1224. https://doi.org/10.1038/s41551-022-00887-1.
47. Wang, J. (2008). Electrochemical Glucose Biosensors. Chem. Rev. ***108***: 814–825. https://doi.org/10.1021/cr068123a.
48. Heller, A., and Feldman, B. (2008). Electrochemical Glucose Sensors and Their Applications in Diabetes Management. Chem. Rev. ***108***(7): 2482–2505. https://doi.org/10.1021/cr068069y.
49. Asarani, N.A.M., Reynolds, A.N., Boucher, S.E., et al. (2020). Cutaneous complications with continuous or flash glucose monitoring use: systematic review of trials and observational studies. J. Diabetes Sci. Technol. ***14***: 328–337. https://doi.org/10.1177/1932296819870849.
50. Swislocki, A.L.M., Krouwer, J., and Ravera, J.J. (2022). Retained Glucose Sensor Wire as a Cause of Leg Pain. Clin. Diabetes ***40***: 247–249. https://doi.org/10.2337/cd21-0059.
51. Kim, N., Kee, S., Lee, S.H., et al. (2014). Highly Conductive PEDOT:PSS Nanofibrils Induced by Solution-Processed Crystallization. Adv. Mater. ***26***: 2268. https://doi.org/10.1002/adma.201304611.
52. Liu, Y., Liu, J., Chen, S., et al. (2019). Soft and elastic hydrogel-based microelectronics for localized low-voltage neuromodulation. Nat. Biomed. Eng. ***3***: 58–68. https://doi.org/10.1038/s41551-018-0335-6.

ACKNOWLEDGMENTS

The authors would like to acknowledge financial support from the National Natural Science Foundation of China (grant nos. T2225010, 32171399, and 32171456); Guangdong Basic and Applied Basic Research Foundation (grant no. 2023A1515011267); Science and Technology Program of Guangzhou, China (grant nos. 2024B03J0121 and 2024B03J1284); the Independent Fund of the State Key Laboratory of Optoelectronic Materials and Technologies (Sun Yat-Sen University) under grant no. OEMT-2022-ZRC-04; and Fundamental Research Funds for the Central Universities, Sun Yat-sen University (no. 24xkjc011). The funders had no role in study design, data collection and analysis, decision to publish, or preparation of the manuscript.

AUTHOR CONTRIBUTIONS

X.L. and X.X. conceived the concept, designed the work, and wrote the manuscript. X.L. performed most of the *in vitro* and *in vivo* experiments. S.Z. and X.H. designed the PCB and assisted in the MN sensor design and fabrication. X.H., C.Y., J.Y., and C.D.Y., assisted in the *in vivo* experiments. M.H. and J.M performed the simulation. X.L., S.Z., J.M., and X.X performed statistical analyses of datasets. X.X. supervised the study. All authors discussed the results and assisted in the preparation of the manuscript. All authors contributed to and approved the manuscript.

DECLARATION OF INTERESTS

The authors declare no competing interests.

SUPPLEMENTAL INFORMATION

It can be found online at https://doi.org/10.1016/j.xinn.2024.100781.